Cellular events of acute, resolving or progressive COVID-19 in SARS-CoV-2 infected non-human primates

Fahlberg MD[1], Blair RV[1,2], Doyle-Meyers LA[1], Midkiff CC[1], Zenere G[1], Russell-Lodrigue KE[1], Monjure CJ[1,2], Haupt EH[1], Penney TP[1], Lehmicke G[1], Threeton BM[1], Golden N[1], Datta PK[1,2], Roy CJ[1,2], Bohm RP[1,2], Maness NJ[1,2], Fischer T[1,2], Rappaport J[1,2], and Vaccari M[1,2*].

[1]Tulane National Primate Research Center, Covington, LA
[2]Tulane University School of Medicine, New Orleans, LA

*To whom correspondence should be addressed:

Monica Vaccari, Ph.D.

Associate Professor, Tulane National Primate Research Center 21 18703

Three Rivers Road, Covington, LA 70433

Email: mvaccari@ tulane.edu

Abstract

We investigated the immune events following SARS-COV-2 infection, from the acute inflammatory state up to four weeks post infection, in non-human primates (NHP) with heterogeneous pulmonary pathology. The acute phase was characterized by a rapid migration of CD16+ monocytes from the blood and concomitant increase in CD16+ macrophages in the lungs. We identified two subsets of interstitial macrophages (HLA-DR+ CD206–), a transitional CD11c+ CD16+ population that was directly associated with IL-6 levels in plasma, and one long lasting CD11b+ CD16+ population. Strikingly, monocytes were a correlate of viral replication in bronchial brushes and levels of TARC (CCL17), and worse disease outcomes were associated with high levels of cell infiltration in lungs and CD11b+ CD16+ macrophages accumulation. Importantly, this accumulation was long-lasting and detectable even in animals with mild or no signs of disease. Interestingly, animals with less signs of disease had a high IL-10:IL-6 ratio. Our results unravel cellular mechanisms of COVID-19 and validate NHP as models to test immune therapies.

The COVID-19 pandemic is a major public health crisis, causing a global medical emergency. There are currently no effective vaccines or drugs approved to completely treat or prevent COVID-19, and much remains unknown about the pathogenesis of the disease. COVID-19 presents with highly variable outcomes, and patients that develop symptoms exhibit a wide range of disease, spanning from mild (fever, cough, shortness of breath) to severe (dyspnea, pneumonia, rapidly progressing radiographic changes)[1]. It is currently estimated that up to 15% of COVID-19 patients progress to acute respiratory distress syndrome (ARDS)[2], which is the major cause of death among fatal SARS-CoV-2 cases.

50

51 Studies elucidating molecular and immunological details of SARS-CoV-2 infection are
52 underway, and many of the reported clinical observations point to the disease being at least
53 partly the result of an excessive host response aimed to clear the virus but instead contributing to
54 disease development[3]. This hypothesis is supported by studies on the closely related coronavirus
55 SARS-CoV-1[4-6], and by clinical reports showing elevated levels of the proinflammatory cytokine
56 IL-6 in SARS-CoV-2 infected patients, particularly among those with severe symptoms[3,7].
57 Interestingly, the increase in IL-6 coincides with the upregulation of chemokines responsible for
58 myelopoiesis and monocyte recruitment to the lungs[3,8] suggesting that peripheral inflammatory
59 monocytes and tissue macrophages may play a role in the cytokine storm seen in severe COVID-
60 19 patients[9]. The underlying inflammatory state and increased myelopoiesis seen in older
61 individuals may be responsible for the high mortality rate seen in this group[10]. A better
62 understanding of immunopathology of COVID-19 will aid the development of targeted
63 immunotherapies and effective vaccines.

64

65

66 Non-human primates (NHP) have been used as animal models to study acute respiratory diseases
67 such as SARS and MERS[11]. In these studies, African green monkeys (AGM) have been shown to
68 be more susceptible to severe disease than rhesus macaques (RM)[12]. Regardless of species
69 differences, and given the overlap between NHP and with human immune systems, both NHP
70 species have been useful models to study host responses to coronaviruses[55]. We and others have
71 shown that both AGM and RM can be successfully infected with SARS-CoV-2 via the intranasal
72 and the intratracheal route, or by aerosol[13-16]. Following exposure, AGM and RM have high

73 levels of virus replication in the respiratory tract for up to two weeks, and both species develop
74 pulmonary pathology characteristic of COVID-19, that varies from very mild to severe[17]. Other
75 groups have described the very early immune events in SARS-CoV-2 infected rhesus macaques,
76 with perturbation of monocytes populations, increased macrophages in lungs, and cellular
77 activation in blood all happening a few days following the infection[18].
78 Here, we extend on these findings by describing the kinetics of immune events following
79 infection, spanning from the acute phase up to four weeks following infection, in the blood and
80 the lungs of four African green monkeys (AGM) and four rhesus macaques (RM) with a
81 heterogeneous spectrum of COVID-19. Overall, we observed a multiphasic mobilization of
82 innate and adaptive cells from the blood to the lung that is strikingly common to both species.
83 The acute inflammatory phase was characterized by an increase in the frequency of monocytes
84 that was positively associated with bronchial viral replication. Consistent with the resolution
85 phase of inflammation in the lung[19] , the second phase was characterized by a switch toward type
86 2 responses in both species. We identified two populations of interstitial macrophages (HLA-
87 DR+ CD206–) in BAL; 1) CD11c+ CD16+ population increasing during the acute phase of
88 infection that was associated with IL-6 levels in the plasma, and 2) a long lasting CD11b+ and
89 CD16+ population accumulating in lungs of both AGM and RM, particularly in those with
90 increased disease severity. Animals with more pronounced clinical signs had a higher level of
91 infiltrates in lungs when compared with animals with no or mild signs, and higher ratio of IL-
92 6:IL-10 (pro-inflammatory: anti-inflammatory) cytokines in plasma.
93 By investigating temporal and spatial changes in immune cells our study links together findings
94 in both NHP and human patients and unravels new cellular events of COVID-19[20,21]. Further, we

validate the use of NHP as a model to study immunopathology and to test immune therapies and vaccines for SARS-CoV-2.

Results

Increased levels of monocytes and chemokines after infection is associated with viral load and disease severity. Four adult RM and four adult AGM were exposed to SARS-CoV-2 by either aerosol or mucosal challenge including buccal, intranasal, intratracheal, and conjunctival (multi-route) exposure (**Supplementary Table 1**). The study concluded at 4 weeks post exposure (**Fig. 1A**)[16]. All eight animals had detectable viral load by RT-PCR on nasal and pharyngeal swabs and bronchial brushes by week 1 (**Fig. 1B**, **Supplementary Table 2**). Viral RNA was also detected in pharyngeal, nasal, buccal, rectal and vaginal swabs. No differences in viral load (VL) were observed between the different routes of exposure or between the two species at week 1. Of note, by week 2 AGM had higher VL than RM in the bronchial brushes and by week 3 VL in RM was mostly undetectable while it remained above detection levels in AGM until study completion (**Fig. 1B** and **Supplementary Table 2**). Similar to humans, the course of disease varied widely across animals, as detailed in **Table 1**. Of the four AGM enrolled, two animals developed severe respiratory signs and were euthanized on days 8 (NC34) and 22 (NC33) post-infection, following established endpoint criteria for NHP study protocols, and as we previously reported[16]. Of the two remaining AGM, NC38 had multifocal mild to moderate interstitial pneumonia scattered throughout all lung lobes and NC40 was mostly asymptomatic and had scant inflammation in all lung lobes at necropsy. Three of the four RM (GH99, HD09, and FR04) developed pneumonia characterized by a granulomatous to pyogranulomatous inflammatory response. This was severe in GH99, mild in HD09, and

119 minimal in FR04. Histopathology of the fourth RM (HB37) revealed a lymphocytic vasculitis
120 and proliferative vasculopathy in the right middle lung lobe. Viral load was not significantly
121 associated with pulmonary pathology, however we observed an inverse association between viral
122 load at week 1 and disease severity ranking (1 to 8 from most severe to least severe) based on the
123 above observations and histopathology findings (AGM: R = 0.8 ; RM: R = –0.4, all animals: P
124 = 0.057, R = – 0.71, by the Spearman correlation test) (**Fig. 1C** and **SF 1A** and **1B**). Clinical
125 signs observed during the course of the study included mild tachypnea (day 11) and cough (day
126 15) in GH99. Intermittent mild to moderate pyrexia was observed in HB37 (day 1-21 post
127 infection). Radiographic changes included a nodule in the right caudal lung lobe (day 11) in
128 GH99, and HD09 also developed a mild, focal increased opacity in the ventral lung field at day
129 11 (**data not shown**).
130 Interestingly, virus-driven immunological changes were remarkably similar between species at
131 this time (**Fig. 1** and **SF 1**). To investigate overall changes driven by viral replication in both
132 groups, we combined their immunological analysis, however at the same time we maintained
133 different specifications for each species (teal = RM and magenta = AGM). Data and statistics are
134 also shown separately per group in **Supplementary Figure 1**. At 1 week after infection both
135 AGM and RM had an increase in the absolute number and frequency of monocytes in the blood
136 (P = 0.065, and P = 0.02 respectively, by the Tukey multiple comparison test, n = 8) compared to
137 baseline levels (**Fig. 1D** and **1E**). This change was significant in AGM alone (absolute number: P
138 = 0.0006, n = 4), and was also observed in all RM, particularly GH99 (**SF 1C-1F)**. The absolute
139 number of neutrophils did not change over time (**SF 1G**). Interestingly, the absolute number of
140 monocytes at week 1 was strongly positively associated with the viral load levels in the bronchial
141 brush samples (P = 0.002, R = 0.93 by the Spearman test) when all the animals were combined

142 (**Fig. 1F**) (AGM: R = 0.8; RM R = 1, not significant in separated group, **SF 1H** and **1I**). We then
143 used the CD14 and CD16 markers to discriminate between three circulating monocytes subtypes:
144 classical (CD14+ CD16–), intermediate (CD14+ CD16+) and non-classical (CD14– CD16+)
145 within the total (HLA-DR+ CD16+ and/or CD14+) monocyte population by flow cytometry
146 (**Fig. 1G - 1I** and **SF 1J- 1N**). At week 1, the frequency of classical monocytes was significantly
147 increased in blood, as seen in humans[22], and the non-classical population was profoundly
148 depleted (increased levels baseline versus week 1: classical P = 0.007 and decreased non-
149 classical P = 0.005 in all animals combined, n = 4) (**Fig. 1H** and **1I**, and **SF 1J- 1K**).
150 Pre-infection levels were restored at 3 weeks post-infection (week 1 vs. week 3: classical P =
151 0.03 and non-classical P = 0.03). These results suggest a rapid and robust recruitment of
152 patrolling monocytes with antiviral activity in tissues following infection in both species.
153 We analyzed a group of eight chemokines known to be involved in the mobilization of innate
154 cells, including monocytes, from the blood to the lung: IP-10 (CXCL-10), MCP-1 (CCL2),
155 MCP-4 (CCL13), Eotaxin, TARC (CCL17), MDC (CCL22), MIP-1a and MIP-1b (**SF 2A-**
156 **2H**). Some of the cytokines measured at baseline in plasma differed between the two species
157 (MCP-4, Eotaxin, MIP-1b and MDC, **Supplementary Table 3** and **SF 2I**). Plasma levels of
158 TARC (CCL17), a ligand for CCR4 that is involved in Th2 cell recruitment[23], were strongly
159 associated with the frequency of monocytes in blood (P = 0.003, R = 0.95, Spearman test,
160 adjusted for multiple comparison: P = 0.02) (**Fig. 1J**). Similarly, TARC was also associated with
161 viral replication in BAL at week 1 (**Fig. 1K** and **SF 2J**) (P = 0.02, R = 0.857, adjusted for
162 multiple comparisons: P = 0.2), as was IP-10 (P = 0.05, R = 0.78, adjusted for multiple
163 comparisons) when all animals were grouped together (**Fig. 1K** and **SF 2K**), a ligand for CXCR3
164 that is associated with disease severity and predicts progression of COVID-19 in humans[24]. To

165 gain a better understanding of a common milieu possibly driving monocyte migration observed
166 in both groups we analyzed changes in the levels of these markers with respect to the baseline.
167 Overall this analysis revealed that animals with the most severe disease outcomes had higher
168 levels of chemokines at week 1, including IP-10, TARC (CCL17) (**Fig. 1L**).
169
170 **Myelomonocytic cells infiltrate BAL and are associated with IL-6.** Influx of macrophages has
171 been observed in the lung of severe cases of COVID-19 in humans[25]. To monitor cell trafficking
172 into the lungs, we collected bronchoalveolar lavage (BAL) at baseline and after each week
173 following infection, up to week 3. As expected, the majority of the cells found in BAL at
174 baseline were alveolar macrophages (AM)[26]. These cells are readily identified by the mannose
175 receptor C type 1 (CD206) marker, express high levels of HLA-DR, and are positive for the
176 scavenger receptor CD163 (**Fig. 2, SF 3A** and **3B**), we observed a decrease in the proportion of
177 AM at week 1 post infection in animals of both species, corresponding with an influx of myeloid
178 HLA-DR+ CD206– CD163– cells (**Fig. 2A** and **2B**, **SF 3C**). Levels of AM similar to pre-
179 infection were restored at week 2 in all but one animal (GH99), and a concomitant increase of
180 CD86 mean fluorescent intensity (MFI) in this population was observed suggesting an M1
181 activation state[27] (**SF 3D**). An increase was also seen in the frequency of CD206+ CD163– non-
182 macrophages that have been previously described as endothelial cells which facilitate
183 lymphocyte trafficking and they are detectable in BAL during inflammatory events (**Fig. 2C**)[28].
184
185 T-distributed stochastic neighbor embedding (tSNE) analysis revealed changes in the phenotype
186 of CD16, CD11b, and CD11c positive populations most prominently at 1-2 weeks post infection
187 (**Fig. 2D - 2F**). In contrast to what we observed in the blood, there was an increase of CD16+
188 HLA-DR+ cells in BAL over time (**Fig. 2G**, and **SF 3E** and **3F**). We observed a transient

189 increase in the level of CD11c+ CD16+ macrophages, which function has been described as
190 patrolling, and they participate in rapid tissue invasion and monocyte survival (baseline vs. week
191 1: P = 0.015) (**Fig. 2H**)[29,30]. The frequency of CD11c+ macrophages in BAL at week 3 was
192 strongly associated with the levels of the proinflammatory IL-6 cytokine in the plasma at the
193 same time point (week 3: P = 0.003, R = 0.96, Spearman test) (**SF 4**). The CD11b marker is
194 required for monocyte migration to sites of inflammation[31], and is highly expressed on myeloid
195 cells recruited from the blood and differentiating into macrophages[32]. We also observed an
196 increase in the percentage of CD11b+ CD16+ HLA-DR+ CD206– macrophages in BAL at week
197 2 and 3 following infection (**Fig. 2I**), a population that is involved in regulating lung
198 inflammatory response[19,27,33,34]. The gating strategy for the two macrophages populations is
199 shown in **Supplementary Figure 3G**.
200
201 **Interstitial macrophages accumulate in lungs of infected animals.** Lungs were collected for
202 all animals at the end of the study, corresponding to 4 weeks post infection (1 week following the
203 last BAL collection shown in Figure 2), with the exception of NC33 and NC34. These two
204 animals had higher levels of IL-6 at necropsy compared to the other six monkeys, and NC34 had
205 symptoms similar to ARDS[16] (**Fig. 3**). Overall, infiltration of macrophages was observed in the
206 lungs of SARS-CoV-2 infected AGM and RM at necropsy and was more robust in animals with
207 severe disease (**Fig. 3A**). We further characterized macrophages population in the lung by
208 staining with the AM marker CD206 (in blue) and with CD11b integrin (in green) and CD16
209 (red) (**Fig. 3B**). Low numbers of macrophages were seen in the lungs of a non-infected control
210 RM, scattered throughout the interstitium and alveolar spaces, as shown by the arrows. In the
211 control this population was bi-morphic and composed of CD11b negative CD16+ CD206–

212 (arrow) in the alveolar septa or CD16+ CD206+ cells within the alveolar spaces (arrowhead)
213 (**Fig. 3B**). In all animals that were infected we could detect CD11b+ CD16+ macrophages. FR04
214 (RM ranking = 7) lungs had macrophages scattered throughout the interstitium and alveolar
215 spaces. The phenotypic population was heterogeneous and contained low numbers of CD11b+
216 CD16+ CD206– macrophages. The most severe RM, GH99 (ranking = 3), had large numbers of
217 macrophages multifocally surrounding small airways denoted by the asterisks. Of note this
218 animal had the higher absolute number of monocytes in the blood at week 1 (**SF 1D**). Low
219 numbers of CD11b+ CD16+ CD206– cells were scattered throughout the predominant
220 population of CD11b+ CD16+ CD206+ macrophages. Macrophages were also scattered
221 throughout the interstitium and alveolar spaces. NC34 and NC33 (AGM ranking = 1 and 2
222 respectively) had multifocal to coalescing areas of hemorrhage (NC33 indicated by the
223 arrows), and pulmonary parenchyma infiltrated by multifocal aggregates of macrophages (NC34)
224 with infiltration by low to moderate numbers of macrophages. The phenotypic population was
225 heterogenous and composed of moderate numbers of CD11b+ CD16+ CD206– macrophages.
226 Altogether these findings present a picture of long-lasting lung inflammation that, albeit more
227 pronounced in animals with severe signs of disease, it is also present in animals with no
228 detectable viral load and mild or no signs of disease after 4 weeks from the infection.
229
230 **NKG2a+ cells and PD-1+ T cells decrease in blood and increase in BAL overtime.**
231 Infiltration of lymphocytes was observed in the lungs of SARS-CoV-2 infected AGM and RM
232 at necropsy and was more robust in animals with severe disease (**Fig. 4A**). We first analyzed the
233 kinetics of innate NK cells subsets, that we defined as HLA-DR– CD3– cells expressing the
234 NKG2a receptors, which are known to traffic to the lung[35] (**Fig. 4B-D**, and **SF 5A** and **5B**)

235 Interestingly, the frequencies of NKG2a+ cells significantly decreased in peripheral blood of
236 both AGM and RM over the course of infection (baseline vs. week 3, P = 0.03) (**Fig. 4B**).
237 Consistent with the pattern described for the myeloid population, we also observed a
238 concomitant increase in the frequencies of NKG2a+ cells in BAL (baseline vs. week 3, P = 0.05)
239 (**Fig. 4C** and **4D**, **SF 5A** and **5B**). Four out of four AGM had decreased NKG2a+ cells in
240 peripheral blood, coinciding with an increase of the same cells in BAL. While the pattern of
241 NKG2a+ cells in peripheral blood of RM was not statistically significant, nonetheless in this
242 species there was a marked increase of those cells in the BAL. These results suggest that the loss
243 of NKG2a+ cells in the PBMCs and the gain of NKG2a+ cells in the BAL may coincide with an
244 egress of these cells from peripheral blood to tissues. Accordingly, the frequency of NKG2a+
245 cells expressing CXCR3, a marker associated with NK cell migration to the lung[36] also
246 significantly decreased in blood over time (baseline vs. week 3, P = 0.03, **Fig. 4E**). Despite this
247 change in lymphocyte phenotype, the absolute number of lymphocytes did not change over the
248 first 2 weeks of infection (**Fig. 4F**) though it is important to note that all 3 remaining AGM had
249 an increase at week 3 (**SF 5C**).
250 tSNE analysis revealed an increase in the level of PD-1 at weeks 2 and 3 post-infection,
251 overlapping with spatial regions corresponding to both CD4+ T and CD8+ T cells (**Fig. 4G**). In
252 fact, the frequency of PD-1+ CD4+ T cells was elevated in the blood of both RM and AGM (**Fig.
253 4H**, and **4I**, respectively). During the first week following the infection we observed an increase
254 in IP-10 and IFN-γ (**SF 5E**), however we also observed a switch toward Th2 type responses
255 characterized by the increase of Th2 cytokines IL-5 and IL-13 over time (**SF 3E**). Accordingly, a
256 gradual increase of Th2 type cells (defined as CXCR3– CCR6 – CD4+ T cells)[37] was seen in the
257 blood within the PD-1 positive population (**Fig. 4J**). The increase of PD-1+ Th2 cells was

258 significantly and positively associated with IL-4 cytokine levels (P = 0.016, R = 0.94, Spearman
259 test) (**SF 5F**). Moreover, we observed an increased level of PD-1+ CD8+ T cells in blood and
260 BAL (BAL: baseline vs. week 2, P = 0.015; baseline vs. week 3, P = 0.03) (data not shown and
261 **Fig. 4K**). Animals divided by species are shown in **SF 5G** and **5H**.
262
263 **The ratio between the anti-inflammatory cytokine IL-10 and the pro inflammatory**
264 **cytokine IL-6 is associated with disease progression.** The pro-inflammatory cytokine IL-6 has
265 been described as a strong predictor to disease progression in humans[3,7]. We measured IL-6 and
266 IL-10 in the plasma of all the animals (**Fig. 5A**). While IL-6 levels alone did not associate with
267 disease severity in NHPs, the ratio of IL-10 to IL-6 levels measured in plasma associated with
268 both the ranking of disease severity and with the pathological score that was obtained by
269 analyzing the extension of the inflammation and edema of the lungs (R = 0.76 P = 0.037; and R
270 = –0.76, P = 0.03, by the Spearman correlation test, all animals) (**Fig. 5B** and **C**). These findings
271 show a complex series of immune events in the lung of that are most likely initiated as a host
272 response to the virus and then evolving overtime toward less antiviral responses, as summarized
273 in **Figure 5D**.
274
275 **DISCUSSION**
276
277 There is an urgent need to develop safe and effective strategies to prevent and treat COVID-19.
278 The development of such strategies requires a clear understanding of the immune cells involved
279 in COVID-19 and their unique role in pathogenesis. Clinical observations in patients and few
280 studies on non-human primates have started to shed light on the immune aspects involved in
281 COVID-19[9,20,38,39]. Here, we further characterized immune events following SARS-CoV-2

282 infection in two NHPs models recapitulating crucial aspects of COVID-19 lung disease[14,16]
283 (**Table 1**). Altogether our findings provide the first evidence in both AGM and RM of a
284 multiphasic immune response characterized by 1) an initial inflammatory phase with monocyte
285 recruitment to the lung 2) a gradual switch from a type 1 to type 2 response, and 3) a "make it or
286 break it" phase with either an increase in anti-inflammatory cytokines IL-10, or IL-6 a pro-
287 inflammatory cytokines associated with disease progression in humans, as summarized in **Figure**
288 **5D**.
289 By examining the temporal and spatial distribution of monocytes and macrophage in blood and
290 BAL and lungs, we confirmed and extended on studies in humans and NHPs suggesting
291 increased myelopoiesis with recruitment of myeloid cells from the blood to lungs during the
292 infection that is initially driven by the virus replicating in the lung[3,14,20]. Similar to what has been
293 described by Wilk *et al.* and Thevarajan *et al.* in humans, we observed an increase of CD14+
294 monocytes, and a corresponding drop in the frequency of CD16+ monocytes in the peripheral
295 blood[20,21]**.** Importantly, we extend on these findings by showing a simultaneous increase in the
296 frequency patrolling CD16+ HLA-DR+ monocytes in BAL occurring in both species and by
297 describing the kinetics of two CD16+ HLA-DR+ CD206– macrophages populations that
298 preferentially populate the alveolar interstitium and exhibit features of antigen-presenting
299 cells[40]: CD11c+ CD16+ cells arising from intravascular CD16+ patrolling monocytes in the
300 acute phase and associating with IL-6 levels, and a CD11b+ macrophage population known to be
301 involved in resolution of inflammation in the lung[19,27,33,34]. The origin and the exact function of
302 these interstitial macrophages remains to be determined.

303 Differently than was observed in humans and previous reported data in RM, we did not detect an
304 increase in the number of neutrophils as these responses may have come up earlier than 1 week
305 after infection as shown by others[18].
306
307
308 Common to both species was the observation that animals with higher levels of myeloid and
309 lymphoid cell infiltration in the lung had worse disease outcomes. Several studies in both SARS-
310 CoV-1 and CoV-2 have reported depleted peripheral NK cell counts in severe patients[9,20,22,38].
311 Our data support the notion of NKG2a+ cell trafficking to the lung during SARS-CoV-
312 2 infection, most likely mediated by IP-10 (CXCL-10), which promotes the recruitment of
313 CXCR3+ Th1 thymocytes and NKs[41,42]. Expression of NKG2a has been linked to both activation
314 and inhibition of inflammation[43]; the function in SARS-CoV-2 remains to be investigated. In the
315 periphery, we also observed increased levels of PD-1 on T cells. This is consistent with findings
316 in humans describing of an exhaustive T cell phenotype during SARS-Cov-1 and Cov-2
317 infection[9,44].
318
319 For the first time, we identified TARC (CCL17) as central to myeloid recruitment in the lung
320 during SARS-CoV-2. Both dendritic cells and CD11b macrophages in the lung have been
321 identified as a source of CCL17 in the airways in other pulmonary inflammatory diseases[45,46].
322 These cells promote the recruitment of T helper type 2 (Th2) lymphocytes into the airway[45].
323 Remarkably, we observed a gradual increase of the recruitment of Th2 lymphocytes into the
324 airway Th2 cell frequency and of Th2 type cytokines such as IL-5, IL-13. These findings show a
325 complex series of immune events in the lung of that are most likely initiated as a host response to
326 the virus, and that they may evolve into other less effective antiviral responses as either an

327 attempt to tissue repair/resolution of inflammation, as summarized in **Figure 5D** or as the result
328 of virus direct immunomodulatory effects on host responses[6].
329
330
331 Intrinsic species-specific susceptibility to disease progression have been described for NHP in
332 SARS-CoV-1[6] with AGM being more susceptible than rhesus to severe disease. There were
333 unexpected similarities in the kinetics and the quality of the immune responses analyzed in RM
334 and AGM, particularly during the acute phase of infection, however AGM did not clear the
335 infection as well as RM and two AGM had most severe symptoms[47]. While the number of
336 animals enrolled in this study was not sufficient to look at species-specific differences and their
337 effect on disease progression, we found that a higher ratio of IL-6:IL-10 cytokine in plasma was
338 associated with disease severity. Undoubtedly, more studies are needed to prove or disprove the
339 single contribution of IL-10 and IL-6 in the outcome of COVID-19 disease and to identify the
340 source of these two potential key players[48].
341
342 Overall, this study uncovers critical steps in the immune events of the host response to SARS-
343 CoV-2 and describes new correlates of viral replication and disease progression. Importantly, we
344 show viral driven inflammation/cell recruitment to the lung occurs rapidly, and lasts up to four
345 weeks post infection, which may explain in part the observed slow recovery from COVID-19
346 seen humans. Finally, these findings have the potential to aid the interpretation of the results of
347 the human trials that are currently underway for several vaccine candidates and may be
348 instrumental in generating new targeted therapeutic strategies aiming at resolving the severe
349 immune deregulation of the lung of COVID-19 patients.
350

351 **Methods**
352
353 **Ethical statement on animal use and SARS-CoV-2 handling.** Animals and infection. The
354 Institutional Animal Care and Use Committee of Tulane University reviewed and approved all
355 the procedures for this study. The Tulane National Primate Research Center is fully accredited
356 by the AAALAC. All animals were cared for in accordance with the ILAR Guide for the Care
357 and Use of Laboratory Animals 8th Edition. The Tulane University Institutional Biosafety
358 Committee approved the procedures for sample handling, inactivation, and transfer from BSL3
359 containment.
360
361 **Animals and infection**. Four adult-aged African green monkeys (Caribbean origin) and four
362 rhesus macaques (Indian ancestry) were exposed to SARS-CoV-2; 2019-nCoV/USA-WA1/2020
363 409 (MN985325.1). The virus stock was prepared in Vero E6 cells and the sequence confirmed
364 by PCR and/or Sanger sequencing. Plaque assays were performed in Vero E6 cells. The rhesus
365 macaques were from the Tulane National Primate Research Center breeding colony pathogen
366 free for simian type D retrovirus (SRV), macacine herpesvirus 1 (B virus), simian
367 immunodeficiency virus (SIV), simian T cell lymphotropic/leukemia virus (STLV), measles
368 virus (MV) and tuberculosis (TB). The African green monkeys were wild caught and at the
369 TNPRC for over a year before being assigned to this study. To mimic different possible routes of
370 infection in humans, animals were exposed to the virus either by aerosol (inhaled dose of 2.0 x
371 10^3 and 2.5 x 10^3 $TCID_{50}$) or by inoculating a cumulative dose of 3.61 x 10^6 PFU through
372 multiple routes (oral, nasal, intratracheal, conjunctival) (**Supplementary Table 1**).
373 The multi route exposure was given to four animals, one adult RM male (GH99, 14 years old),
374 one adult RM female (HD09, 13 years old) and two AGM, one aged male (NC40, 16 years old,
375 approximately) and one aged female (NC33, 16 years old, approximately). An additional two

376 adult males RM (FR04 and HB37, 15 and 13 years old, respectively) and one aged male and
377 female AGM: NC34 and NC38 (16 years old, approximately) were exposed by aerosol
378 (**Supplementary Table 1**).
379
380 **Cell count and CO_2 and SpO_2 pressure measurements.** Total white blood cell counts, white
381 blood cell differentials, red blood cell counts, platelet counts, hematocrit values, total
382 hemoglobin concentrations, mean cell volumes, mean corpuscular volumes, and mean
383 corpuscular hemoglobin concentrations were analyzed from blood collected in tubes containing
384 EDTA using a SYSMEX XN-1000v Hematology Analyzer in the Level 2 Lab and a Sysmex XS-
385 1000 in the Level 3 Lab. CO_2 measurements were taken using the Piccolo Express Chemistry
386 Analyzer in the Level 3 lab and is part of the Metabolic Comprehensive Panel. SpO_2 values were
387 obtained using the Masimo Rad-57 Handheld Pulse Oximeter.
388
389 **Sample collection and processing.** Blood EDTA was collected by venipuncture and bronchial
390 brush and BAL by bronchoscopy. For the latter, the bronchoscope is introduced into the trachea
391 and directed into one of the bronchi. The bronchoscope is advanced to the point where the
392 diameter of the bronchoscope approximates the dimensions of the bronchus. The bronchial brush
393 is passed through the channel of the bronchoscope. The brush is gently advanced until the lumen
394 of the bronchus or bronchioles approximates the dimensions of the brush. The brush is then be
395 gently advanced back and forth against the mucosa to gather cells. The brush is removed from
396 the channel of the bronchoscope and the brush is placed into 200 µL of DNA/RNA Shield X1
397 (Cat.# R1200, Zymo Research, Irvine, CA). The bronchoscope remains in place while two
398 aliquots of 20 ml of saline each are instilled into the bronchus and subsequently aspirated. This
399 procedure is then repeated in the opposite lung.

400

401 Blood was layered over Ficoll-Plaque Plus (GE Healthcare17144003) and centrifuged for 30
402 minutes in cap-locked adaptors. Differential migration of cells during centrifugation results in
403 the formation of layers containing different cell types and allows collection of peripheral blood
404 mononuclear cells (PBMCs) from other populations. PBMCs were collected, counted and
405 aliquoted in tubes or resuspended in freezing media containing Fetal Bovine Serum and DMSO.
406 For bronchoalveolar lavage (BAL), cells and supernatant were separated by centrifugation (15
407 minutes at 2,000 x g at RT) in cap-locked adaptors and cells were lysed in Ammonium Chloride
408 Potassium (ACK) lysing buffer at room temperature for 5 minutes (Gibco# A1049201) washed
409 in 2% FBS, and resuspended in PBS and counted under laminar flux hood in BCL3. Fresh cells
410 were stained for flow cytometry.

411

412 **BAL and PBMCs staining.** Freshly obtained PBMCs and cells obtained from BAL were stained
413 with appropriate antibody cocktails and incubated for 30 minutes at room temperature.
414 Antibodies are listed in **Supplementary Table 4.** Cells were fixed with 4% or 2% PFA-BSA
415 overnight. Samples were run on a FACSAria Fusion flow cytometer (Becton Dickinson) within a
416 Biosafety Cabinet, and each sample was run for at least five minutes. For all panels, the
417 LIVE/DEAD Fixable Aqua Dead cell Stain kit was used (ThermoFisher #L34957). Alveolar
418 macrophages were gated based on the size and the expression of HLA-DR, CD206 and CD163
419 markers. Myeloid infiltrates were gated as cells negative for CD206 and CD163 and positive for
420 HLA-DR, CD16 and CD11b. The gating strategy is shown in **Supplementary Figure 3G**.
421 NKG2a+ cells were gated on the CD3 negative parent population. Th1, Th2, and Th17 cells were
422 gated as previously described[37]. tSNE analyses were performed in FlowJo using the opt-SNE
423 algorithm and designed in R using the ggplot2 package[49].

424
425 **Histopathology and scoring.** Tissue samples were fixed in Z-fix (Anatech), embedded in
426 paraffin and 5 μm thick sections were cut, adhered to charged glass slides and stained with
427 hematoxylin and eosin. All slides were scanned on a Zeiss Axio Scan.Z1 digital slide scanner.
428 Images were acquired using HALO software (Indica Labs). Quantification of pathologic lesions
429 was performed with HALO software. Machine learning (Random Forest) algorithms were
430 trained by a board -certified pathologist to recognize fluidic and cellular inflammation in the
431 lungs of the RM and AGM. Scores were assigned to fluidic and cellular inflammation,
432 separately, based on the percentage of lung affected. Fluidic and cellular inflammation scores
433 were summated for all lobes and animals were ranked from 1 (highest sum) to 8 (lowest sum).
434
435 **Plasma cytokines and chemokines.** Plasma was collected by spinning and was thawed before
436 use. Cytokines were measured using 497 Mesoscale Discovery. IFN-γ, IL-4, IL-6, IL-8, IL-10
437 and IL-13 were part of the V-Plex Proinflammatory Panel 1, 10-Plex. V-plex. The chemokine
438 panel (#K15049D, Mesoscale Discovery, Rockville, Maryland) was also used, following the
439 instructions of the kit. The plate was read on a MESO Quickplex 500 SQ120 machine.
440 Heatmaps were generated using the 'pheatmap' package in R[50,51]. Data were normalized by
441 dividing raw values at week 1 by baseline values for each animal, followed by the application of
442 $\log_2$. Values below the limit of detection were replaced with the lowest limit of detection value
443 based on the standard curve for each run, or with the lowest value detected during the run,
444 whichever was smaller. Bubble plots were generated using the 'ggplot2' package in R, using the
445 same normalized data shown in the heatmap[49]. Scatter plots were drawn using raw data points
446 and display Pearson's correlation coefficients and a 95% confidence interval.
447

448 **RNA isolation**. Swab and bronchial brush samples were collected in 200 µL of
449 DNA/RNA Shield X1 (Cat.# R1200, Zymo Research, Irvine, CA) and extracted for
450 Viral RNA (vRNA) using the Quick-RNAViral kit (Cat.# R1034/5, Zymo Research). The Viral
451 RNA Buffer dispensed directly to the swab in the DNA/RNA Shield. The swab was directly
452 inserted into the spin column. The vRNA was eluted (45µL) and 5 µL was added in a 0.1 mL fast
453 96-well optical microtiter plate (Cat.# 4346906, ThermoFisher, CA).
454
455 **Viral RNA detection.** RT-qPCR reaction TaqPath1-Step MultiplexMaster Mix was used (Cat.#
456 A28527, ThermoFisher) along with the 2019-nCoV RUO Kit (Cat.# 10006713, IDTDNA,
457 Coralville, IA) targeting the N1 amplicon of N gene of SARS2-nCoV19 (accession
458 MN908947). The master mix was added to the microtiter plates covered with optical film (cat.
459 #4311971; ThermoFisher) and then was vortexed and pulse centrifuged. The RT-qPCR
460 program consisted of incubation at 25°C for 2 minutes, RT
461 incubation at 50°C for 15 minutes, and an enzyme activation at 95°C for 2 minutes followed
462 by 40 cycles of denaturing step at 95°C for 3 seconds and annealing at 60°C for 30 seconds.
463 Fluorescence signals were detected with an Applied Biosystems QuantStudio6
464 Sequence Detector. Data were captured and analyzed with Sequence Detector Software v1.3
465 (Applied Biosystems, Foster City, CA). Viral copy numbers were calculated by plotting Cq
466 Values obtained from unknown (i.e. test) samples against a standard curve representing known
467 viral copy numbers. The limit of detection of the assay was 10 copies per reaction volume. A
468 2019-nCoVpositive control (Cat.#10006625, IDTDNA) were analyzed in parallel with every set
469 of test samples. A non-template control (NTC) was also included.
470

471 **Immunohistochemistry.** 5 μm sections of Formalin-fixed, paraffin-embedded lung were
472 mounted on charged glass slides, baked overnight at 56$_{o}$C and passed through Xylene, graded
473 ethanol, and double distilled water to remove paraffin and rehydrate tissue sections. A
474 microwave was used for heat induced epitope retrieval. Slides were heated in a high pH solution
475 (Vector Labs H-3301), rinsed in hot water and transferred to a heated low pH solution (Vector
476 Labs H-3300) where they were allowed to cool to room temperature. Once cool, slides were
477 incubated with Background Punisher (Biocare Medical BP974H) for 10 minutes, washed and
478 incubated with serum free protein block (Dako X0909) for 20 minutes. Immediately following
479 blocking, a mouse anti-CD16 primary antibody was diluted in the serum free protein block and
480 added to the slides for 60 minutes. Slides were washed and a MACH3 AP kit (Biocare Medical
481 M3M532) was used to label the primary antibody. Both the MACH3 mouse probe and polymer
482 were incubated for 20 minutes with washes in between. Signal was developed with Permanent
483 Red substrate (Dako K0640) for 13 minutes to allow for visualization of the CD16+ cells. Slides
484 were thoroughly washed and incubated with a blocking buffer comprised of 1% normal donkey
485 serum (NDS) for 40 minutes. A rabbit anti-CD11b primary antibody was diluted in NDS and
486 added to the slides for 60 minutes. After washing, slides were incubated for 40 minutes with a
487 fluorescently tagged secondary antibody. The staining process was then repeated, on all slides,
488 for the labeling of CD206. Following washes, DAPI (4',6-diamidino-2-phenylindole) was used
489 to label the nuclei of each section. Slides were mounted using a homemade anti-quenching
490 mounting media containing Mowiol (Calbiochem #475904) and DABCO (Sigma #D2522) and
491 imaged with a Zeiss Axio Slide Scanner. Antibodies are shown in **Supplementary Table 4.**
492

493 **Statistical analysis.** Correlation analyses were performed using the non-parametric Spearman
494 rank correlation method (two-tailed, 95% confidence) using exact permutation P values when
495 ranks were used, or Peason's correlation test when both variables were continuous. Analysis of
496 variance (ANOVA) was used for comparing statistical differences between multiple groups,
497 followed by Dunn's multiple comparison tests. Kruskal-Wallis ANOVA or Mann-Whitney tests
498 were used. All statistical analyses were performed using GraphPad Prism (version 8.4.2
499 GraphPad Software, La Jolla California USA) and R software (URL http://www.R-
500 project.org/). Correlation plots were created using the 'Performance Analytics' and 'corrr' plots,
501 respectively, in R[51-53].

502 **Acknowledgments**

503 We would like to thank Dr. Joseph (JC) Mudd and Dr. Cariappa Annaiah for critical reading of
504 the manuscript and Amitinder (Miti) Kaur, Megan Varnado, Kaitlin Didier from the TNPRC
505 Flow Cytometry Core for their help. We thank Angela Birnbaum for reviewing and optimizing
506 all technical SOPs and overseeing the safety of this study.
507 We would also like to thank Fast Grant Funding for COVID-19 Science for partially funding this
508 work and the NIH for supporting this work through the TNPRC base grant (P51 OD011104 59).
509

510 **Competing Interests statement**
511

512 These authors declare no competing interests.

513
514 **Author Contributions**
515 MDF analyzed data composed figures and wrote the manuscript,
516 BRV was the lead pathologist and LADM was the project veterinarian, contributed to study design, and
517 writing of the IACUC and manuscript. CCM designed IHC panels and performed the IHC staining, GZ
518 wrote the manuscript, KERL was a project veterinarian, made clinical assessments and collected samples,
519 CJM processed and analyzed samples for RT-qPCR, contributed; EHH provided the mesoscale data, TPP
520 stained the samples with GL and BMT. GL contributed to study design, provided administrative support,
521 and aided with sample processing and archiving. NG contributed to study design, study coordination,
522 sample processing, and SOP development. PKD processed and analyzed viral load data. CJR conceived
523 and performed aerosol experiments. RPB contributed to study design, analysis of clinical and imaging
524 results, and writing the manuscripts. NJM performed staining of BAL and contributed to writing the
525 manuscript. TF contributed to the animal study design and planning and contributed to writing the
526 manuscript. JR designed and supported the animal study and helped with the writing of the manuscript.
527 MV conceived and supported the study, run experiments, analyzed data and wrote the manuscript.

REFERENCES

1. Guan, W.J., *et al.* Clinical Characteristics of Coronavirus Disease 2019 in China. *N Engl J Med* **382**, 1708-1720 (2020).
2. Sun, P., *et al.* Clinical characteristics of hospitalized patients with SARS-CoV-2 infection: A single arm meta-analysis. *J Med Virol* **92**, 612-617 (2020).
3. Blanco-Melo, D., *et al.* Imbalanced Host Response to SARS-CoV-2 Drives Development of COVID-19. *Cell* **181**, 1036-1045.e1039 (2020).
4. Weiss, S.R. Forty years with coronaviruses. *J Exp Med* **217**(2020).
5. Clay, C., *et al.* Primary severe acute respiratory syndrome coronavirus infection limits replication but not lung inflammation upon homologous rechallenge. *J Virol* **86**, 4234-4244 (2012).
6. Graham, R.L., Donaldson, E.F. & Baric, R.S. A decade after SARS: strategies for controlling emerging coronaviruses. *Nat Rev Microbiol* **11**, 836-848 (2013).
7. Ruan, Q., Yang, K., Wang, W., Jiang, L. & Song, J. Clinical predictors of mortality due to COVID-19 based on an analysis of data of 150 patients from Wuhan, China. *Intensive Care Med* **46**, 846-848 (2020).
8. Xiong, Y., *et al.* Transcriptomic characteristics of bronchoalveolar lavage fluid and peripheral blood mononuclear cells in COVID-19 patients. *Emerg Microbes Infect* **9**, 761-770 (2020).
9. Zhou, Y., *et al.* Pathogenic T cells and inflammatory monocytes incite inflammatory storm in severe COVID-19 patients. *National Science Review* (2020).
10. Crooke, S.N., Ovsyannikova, I.G., Poland, G.A. & Kennedy, R.B. Immunosenescence and human vaccine immune responses. *Immun Ageing* **16**, 25 (2019).
11. Gretebeck, L.M. & Subbarao, K. Animal models for SARS and MERS coronaviruses. *Curr Opin Virol* **13**, 123-129 (2015).
12. McAuliffe, J., *et al.* Replication of SARS coronavirus administered into the respiratory tract of African Green, rhesus and cynomolgus monkeys. *Virology* **330**, 8-15 (2004).
13. Chandrashekar, A., *et al.* SARS-CoV-2 infection protects against rechallenge in rhesus macaques. *Science* (2020).
14. Singh, D.K., *et al.*
15. Yu, J., *et al.* DNA vaccine protection against SARS-CoV-2 in rhesus macaques. *Science* (2020).
16. Blair, R.V., *et al.* ARDS and Cytokine Storm in SARS-CoV-2 Infected Caribbean Vervets. *BioRxiv* (2020).
17. Munster, V.J., *et al.* Respiratory disease in rhesus macaques inoculated with SARS-CoV-2. *Nature* (2020).
18. Singh, D.K., *et al.* SARS-CoV-2 infection leads to acute infection with dynamic cellular and inflammatory flux in the lung that varies across nonhuman primate species. *BioRxiv* (2020).
19. Aggarwal, N.R., King, L.S. & D'Alessio, F.R. Diverse macrophage populations mediate acute lung inflammation and resolution. *Am J Physiol Lung Cell Mol Physiol* **306**, L709-725 (2014).

573 20. Wilk, A.J., *et al.* A single-cell atlas of the peripheral immune response in patients with
574 severe COVID-19. *Nat Med* (2020).
575 21. Thevarajan, I., *et al.* Breadth of concomitant immune responses prior to patient recovery:
576 a case report of non-severe COVID-19. *Nat Med* **26**, 453-455 (2020).
577 22. Wen, W., *et al.* Immune cell profiling of COVID-19 patients in the recovery stage by
578 single-cell sequencing. *Cell Discov* **6**, 31 (2020).
579 23. Anderson, C.A., *et al.* A degradatory fate for CCR4 suggests a primary role in Th2
580 inflammation. *J Leukoc Biol* **107**, 455-466 (2020).
581 24. Yang, Y., *et al.* Plasma IP-10 and MCP-3 levels are highly associated with disease
582 severity and predict the progression of COVID-19. *J Allergy Clin Immunol* (2020).
583 25. Pence, B.D. Severe COVID-19 and aging: are monocytes the key? *Geroscience* (2020).
584 26. Cai, Y., *et al.* In vivo characterization of alveolar and interstitial lung macrophages in
585 rhesus macaques: implications for understanding lung disease in humans. *J Immunol* **192**,
586 2821-2829 (2014).
587 27. Johnston, L.K., Rims, C.R., Gill, S.E., McGuire, J.K. & Manicone, A.M. Pulmonary
588 macrophage subpopulations in the induction and resolution of acute lung injury. *Am J*
589 *Respir Cell Mol Biol* **47**, 417-426 (2012).
590 28. Irjala, H., *et al.* Mannose receptor is a novel ligand for L-selectin and mediates
591 lymphocyte binding to lymphatic endothelium. *J Exp Med* **194**, 1033-1042 (2001).
592 29. Auffray, C., *et al.* Monitoring of blood vessels and tissues by a population of monocytes
593 with patrolling behavior. *Science* **317**, 666-670 (2007).
594 30. Landsman, L., *et al.* CX3CR1 is required for monocyte homeostasis and atherogenesis by
595 promoting cell survival. *Blood* **113**, 963-972 (2009).
596 31. Prieto, J., Eklund, A. & Patarroyo, M. Regulated expression of integrins and other
597 adhesion molecules during differentiation of monocytes into macrophages. *Cell Immunol*
598 **156**, 191-211 (1994).
599 32. Tam, J.W., Kullas, A.L., Mena, P., Bliska, J.B. & van der Velden, A.W. CD11b+ Ly6Chi
600 Ly6G- immature myeloid cells recruited in response to Salmonella enterica serovar
601 Typhimurium infection exhibit protective and immunosuppressive properties. *Infect*
602 *Immun* **82**, 2606-2614 (2014).
603 33. Liao, M., *et al.* Single-cell landscape of bronchoalveolar immune cells in patients with
604 COVID-19. *Nat Med* **26**, 842-844 (2020).
605 34. Steinmüller, C., Franke-Ullmann, G., Lohmann-Matthes, M.L. & Emmendörffer, A.
606 Local activation of nonspecific defense against a respiratory model infection by
607 application of interferon-gamma: comparison between rat alveolar and interstitial lung
608 macrophages. *Am J Respir Cell Mol Biol* **22**, 481-490 (2000).
609 35. Cong, J. & Wei, H. Natural Killer Cells in the Lungs. *Front Immunol* **10**, 1416 (2019).
610 36. Carlin, L.E., Hemann, E.A., Zacharias, Z.R., Heusel, J.W. & Legge, K.L. Natural Killer
611 Cell Recruitment to the Lung During Influenza A Virus Infection Is Dependent on
612 CXCR3, CCR5, and Virus Exposure Dose. *Front Immunol* **9**, 781 (2018).
613 37. Vaccari, M., *et al.* HIV vaccine candidate activation of hypoxia and the inflammasome in
614 CD14. *Nat Med* **24**, 847-856 (2018).
615 38. National Research Project for SARS, B.G. The involvement of natural killer cells in the
616 pathogenesis of severe acute respiratory syndrome. *Am J Clin Pathol* **121**, 507-511
617 (2004).

618 39. Kuri-Cervantes, L., *et al.* Immunologic perturbations in severe COVID-19/SARS-CoV-2
619 infection. *bioRxiv* (2020).
620 40. Schyns, J., *et al.* Non-classical tissue monocytes and two functionally distinct populations
621 of interstitial macrophages populate the mouse lung. *Nat Commun* **10**, 3964 (2019).
622 41. Jiang, D., *et al.* Regulation of pulmonary fibrosis by chemokine receptor CXCR3. *J Clin*
623 *Invest* **114**, 291-299 (2004).
624 42. Agostini, C., *et al.* Cxcr3 and its ligand CXCL10 are expressed by inflammatory cells
625 infiltrating lung allografts and mediate chemotaxis of T cells at sites of rejection. *Am J*
626 *Pathol* **158**, 1703-1711 (2001).
627 43. Creelan, B.C. & Antonia, S.J. The NKG2A immune checkpoint - a new direction in
628 cancer immunotherapy. *Nat Rev Clin Oncol* **16**, 277-278 (2019).
629 44. Li, C.K., *et al.* T cell responses to whole SARS coronavirus in humans. *J Immunol* **181**,
630 5490-5500 (2008).
631 45. Medoff, B.D., *et al.* CD11b+ myeloid cells are the key mediators of Th2 cell homing into
632 the airway in allergic inflammation. *J Immunol* **182**, 623-635 (2009).
633 46. Alferink, J., *et al.* Compartmentalized production of CCL17 in vivo: strong inducibility in
634 peripheral dendritic cells contrasts selective absence from the spleen. *J Exp Med* **197**,
635 585-599 (2003).
636 47. Woolsey, C., *et al.* Establishment of an African green monkey model for COVID-19.
637 *bioRxiv* (2020).
638 48. Han, H., *et al.* Profiling serum cytokines in COVID-19 patients reveals IL-6 and IL-10
639 are disease severity predictors. *Emerg Microbes Infect* **9**, 1123-1130 (2020).
640 49. Wickham, H. ggplot2: Elegant Graphics for Data Analysis. (Springer-
641 Verlag, New York, 2016).
642 50. Kolde, R. pheatmap: Pretty Heatmaps (2018).
643 51. Team, R.C. R: A language and environment for statistical computing. . (Foundation for
644 Statistical Computing, Vienna, Austria, 2019).
645 52. Peterson, B.G. & Carl, P. PerformanceAnalytics: Econometric Tools for Performance
646 and Risk Analysis. . (2020).
647 53. Kuhn, M., Jackson, S. & Cimentada, J. corrr: Correlations in R. (2020).
648
649
650 ## Figure Legend
651
652 **Figure 1. Monocytes are a correlate of bronchoalveolar viral replication.** (**A**) Schematic of
653 study design. Arrows represent time of inoculation with SARS-CoV-2 (day 0) or sacrifice (up to
654 28 days post infection). Unless stated otherwise, rhesus macaque data are shown in teal, and
655 African green monkey data are shown in magenta. (**B**) SARS-CoV-2 RNA levels in bronchial
656 brushes over time. (**C**) Association between SARS-CoV-2 load in bronchial brushes and ranking
657 of disease severity in all eight animals (most severe case = 1; mildest case = 8). (**D**) Changes in

658 monocyte count in blood before and after infection. (**E**) Proportion of total monocytes (HLA-
659 DR+ CD16+ and/or CD14+ out of CD45+ leukocytes) in PBMCs over time. (**F**) Correlation
660 between SARS-CoV-2 viral load in bronchial brushes and absolute count of monocytes in blood
661 at one-week post-infection (1wk pi). (**G**) Representative flow cytometry changes in non-
662 classical monocytes after the infection in blood (1wk pi). (**H**) Percent of classical (CD14+
663 CD16–) and (**I**) non classical monocytes (CD14– CD16+) out of total monocytes in PBMCs. (**J**)
664 Correlation between monocytes absolute numbers in blood and TARC (CCL17) in plasma (1wk
665 pi). (**K**) Relationship between fold change of chemokines and SARS-CoV-2 viral load in
666 bronchoalveolar brushes (1wk pi). (**L**) Heatmap displaying log2 fold-change of 8 chemokines
667 involved with traffic of monocytes to the lung. (1wk pi). Animals are ordered by ranking of
668 disease severity.
669
670 **Figure 2. Myelomonocytic cells increase in BAL is associated with IL-6.** (**A**) Decrease of
671 alveolar macrophages (HLA-DR+ CD206+ CD163+ cells) in the BAL after infection. (**B**)
672 Increase in the frequency of myelomonocytic infiltrates (HLA-DR+ CD206– CD163–) and (**C**)
673 of endothelial cells (HLA-DR+ CD206– CD163+) at infection in BAL (1wk pi). (**D**) tSNE plots
674 displaying kinetics of expression of CD16, CD11b and CD11c markers on live/ HLA-DR+ cells
675 populations in BAL before and after infection. (**E**) Gating of CD11c+ and CD11b+ populations
676 on the tSNE map based on antigen expression and discrete density clustering. (**F**)
677 Characterization of populations shown in (**E**). The heatmap depicts fold-change values of each
678 antigen compared to channel values of negative-expressing cell populations. (**G**) Increase in the
679 percentage of CD16+ HLA-DR+ cells and (**H**) in the percentage of interstitial macrophages
680 (CD16+ CD206– HLA-DR+) expressing of CD11c and (**I**) CD11b in BAL overtime.

681

682 **Figure 3. Interstitial macrophages are increased in the lung of SARS-CoV-2 infected**
683 **animals.** (**A**) Macrophage infiltration varied from minimal to severe in both rhesus and AGM
684 infected with SARS-CoV-2. (**B**) Fluorescent immunohistochemistry in the lung of AGM and
685 RM showing infiltration of CD16+ CD11b+ CD206– macrophages (arrows), with lesser
686 numbers of CD16+ CD206+ macrophages (arrowheads). Inset showing a higher magnification
687 of CD16+ CD11b+ CD206–macrophages (arrows). Asterix shows macrophages multifocally
688 surrounding small airways in GH99. White: DAPI (nuclei); Green: CD11b; Red: CD16; Blue:
689 CD206.

690

691 **Figure 4. Lymphocytes infiltration in the lungs is associated with disease severity.** (**A**)
692 Histopathologic findings showing infiltration of lymphocytes in the lung of AGM (NC40 and
693 NC34) and RM (FR04 and GH99) with mild (NC40 and FR04), moderate (GH99), and severe
694 disease (NC34). (**B**) Frequency of NKG2a+ cells in the blood or (**C**) BAL of 4 AGM and 4 RM
695 at baseline, 2 weeks and 3 weeks post SARS-CoV-2 infection by flow cytometry. (**D**)
696 Representative flow cytometry plot showing decreased frequency of NGK2a+ cells in PBMCs
697 and increased frequency in BAL to baseline in at week 3 post SARS-CoV-2 infection respect to
698 baseline. One animal for each species is shown. (**E**) Decrease in the frequency of CXCR3+
699 NKG2a+ cells in the blood at 2 weeks, and 3 weeks post SARS-CoV-2 infection compared to the
700 baseline. (**F**) Absolute number of lymphocytes before and after infection. (**G**) tSNE plots
701 displaying kinetics of PD-1 expression (in red) on lymphocytic cell populations over time. (**H**)
702 Frequency of PD-1+ Th2 (CXCR3– CCR6–) CD4+ T cells is increased in RM and (**I**) in AGM
703 overtime following the infection. (**J**) Changes in the percentage of Th2 (purple), Th1 (blue) and

704 Th17 (grey) cells within the total PD-1+ CD4+ T cell population. (**K**) Significant increase in the

705 percentage of PD-1+ CD8+ T cells in BAL.

706

707 **Figure 5. Increased IL-6 in the absence of IL-10 is associated with disease progression.**

708 Levels of IL-6 and IL-10 in plasma overtime (pg/ml) **(A)** and **(B)** correlation between the ratio of

709 IL-10 to IL-6 levels measured in plasma and the ranking of disease severity. (**C)** Levels of IL-6

710 and IL-10 after infection in plasma (pg/ml) in individual animals. (**D**) Summary of immune

711 events in lungs and blood of SARS-CoV-2 infected animals, from the 1-acute phase 2- switch to

712 Th2 type responses and 3- resolution phase.

713

714

715
716
717
718 **Table 1: Heterogeneous clinical and pathological outcomes following SARS-CoV-2 infection**

Animal ID	Clinical Findings	Clinical Score	Pathology Findings	Pathology Score	Ranking
NC34	Severe reduction in SpO_2, moderate tachypnea, and severe hypothermia just prior to euthanasia for severe respiratory distress at 8 days post infection. Less than 24 hours earlier, the only abnormality was a moderate reduction in SpO_2. Radiography appeared unremarkable until euthanasia when moderate to severe alveolar pattern with lobar sign and air bronchograms in right lung fields was observed.	9	Bronchointerstitial lung pattern in all lobes that was most severe in the right caudal lung lobe. Microscopically all lung lobes exhibited similar changes with the right caudal and right accessory lung lobe being the most severely affected. The lung lesions were comprised of diffuse alveolar damage with hyaline membrane formation, type II pneumocyte hyperplasia, and rare multinucleated giant syncytia. Some regions showed early evidence of organizing pneumonia and fibrosis.	19	1
NC33	Severe reduction in SpO_2, severe tachypnea, and severe hypothermia just prior to euthanasia for severe respiratory distress at 22 days post infection. Less than 24 hours earlier, the only abnormality was a mild reduction in SpO_2. Radiography appeared unremarkable until euthanasia when moderate to severe alveolar pattern in right middle/caudal lung fields and mild alveolar pattern left caudal lung fields were observed.	10	Severe diffuse alveolar damage of the right lower lung lobe. Other lobes exhibited suppurative alveolar infiltrate with lesser fibrin and edema. The right lung lobe contains peracute to acute lesions of necrosis, fibrin, and hemorrhage with minimal cellular infiltrate.	14	2
GH99	Transient cough beginning on 15 days post infection. Radiography showed significant changes at 11 days post infection which improved through 27 days post infection.	1	Severe bronchopneumonia of the right lower lung with granulomatous to pyogranulomatous inflammatory response.	10	3
NC38	Minor intermittent reductions in SpO_2	0	Mild interstitial pneumonia with low numbers of multinucleated giant cells and rare atypical pneumocyte hyperplasia.	8	4
HD09	Mild focal increase opacity ventral lung field at 11 days post infection.	1	Minimal to mild inflammation scattered throughout the lungs.	9	5
HB37	Intermittent mild to moderate pyrexia from 1-21 days post infection with mild dehydration from 14-21 days post infection.	1	Proliferative lymphocytic vasculitis and proliferative vasculopathy in the right middle lung lobe. Scattered interstitial inflammation throughout the remaining lung lobes.	5	6
FR04	Unremarkable	0	Bronchioles exhibited multifocal, mild mineralization.	6	7
NC40	Minor intermittent reductions in SpO_2	1	Minimal changes within lungs. Mild multifocal thickening of the alveolar septa in the right lower lobe associated with a mild inflammatory infiltrate.	4	8

719
720

721 Clinical findings are summarized for the duration of infection. Clinical scores, pathology findings,
722 and pathology scores reflect measurements at time of necropsy. Rankings were determined based
723 on a combination of the clinical findings and scores throughout the duration of infection and the
724 pathology findings and scores at time of necropsy (1 = severe; 8 = mild).
725 SpO_2 = oxygen saturation.
726
727

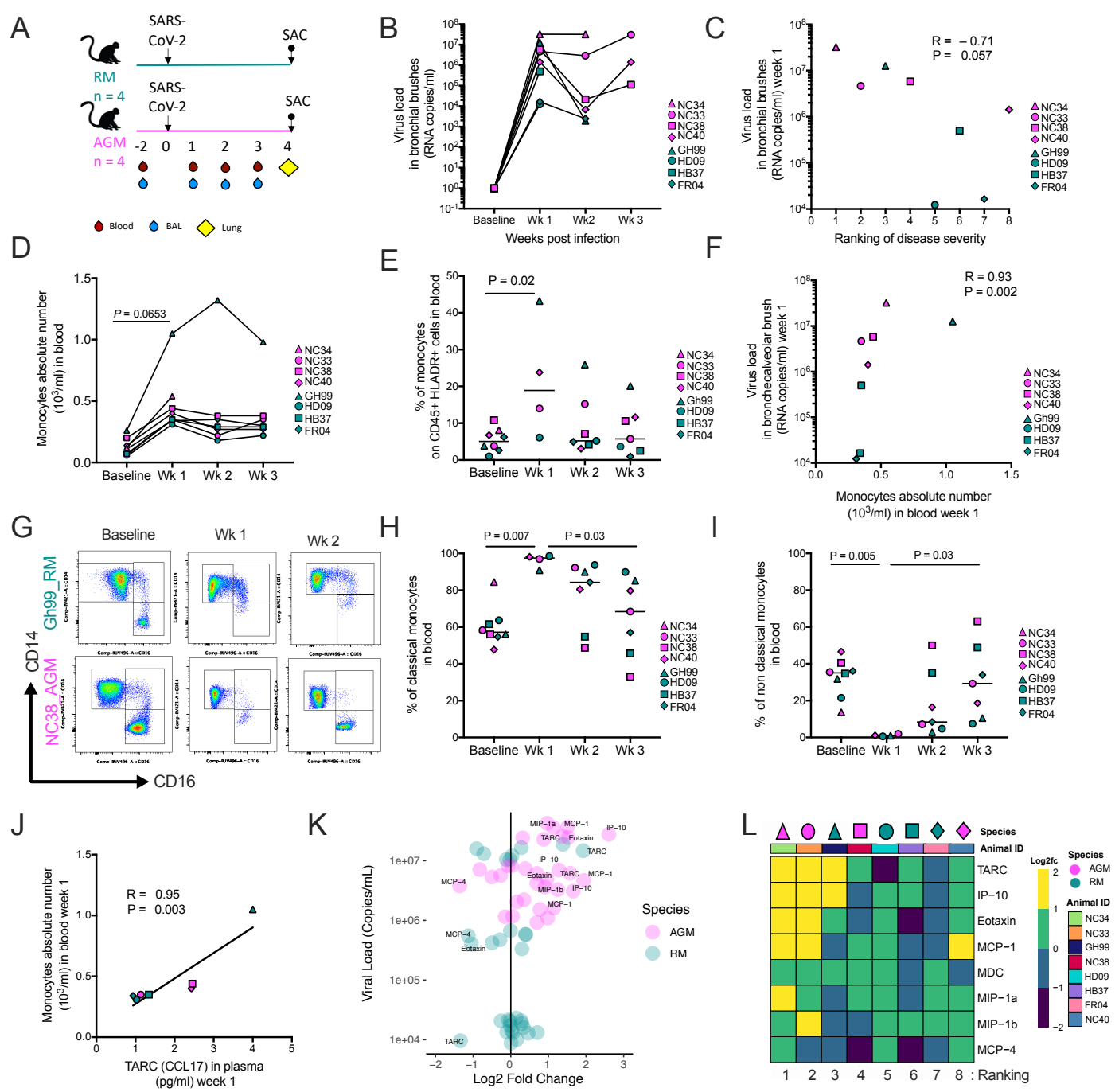
A
SARS-CoV-2
SAC
RM
n = 4
SARS-CoV-2
SAC
AGM
n = 4
-2 0 1 2 3 4
Blood
BAL
Lung
B
Virus load in bronchial brushes (RNA copies/ml)
Baseline
Wk 1
Wk2
Wk 3
Weeks post infection
NC34
NC33
NC38
NC40
GH99
HD09
HB37
FR04
C
R = −0.71
P = 0.057
Virus load in bronchial brushes (RNA copies/ml) week 1
Ranking of disease severity
D
P = 0.0653
Monocytes absolute number (10³/ml) in blood
Baseline
Wk 1
Wk 2
Wk 3
E
P = 0.02
% of monocytes on CD45+ HLADR+ cells in blood
F
R = 0.93
P = 0.002
Virus load in broncheoalveolar brush (RNA copies/ml) week 1
Monocytes absolute number (10³/ml) in blood week 1
G
Baseline
Wk 1
Wk 2
Gh99_RM
NC38_AGM
CD14
CD16
H
P = 0.007
P = 0.03
% of classical monocytes in blood
I
P = 0.005
P = 0.03
% of non classical monocytes in blood
J
R = 0.95
P = 0.003
Monocytes absolute number (10³/ml) in blood week 1
TARC (CCL17) in plasma (pg/ml) week 1
K
Viral Load (Copies/mL)
Log2 Fold Change
MIP−1a
MCP−1
IP−10
TARC
Eotaxin
MCP−4
MIP−1b
Species
AGM
RM
L
Species
Animal ID
TARC
IP−10
Eotaxin
MCP−1
MDC
MIP−1a
MIP−1b
MCP−4
Log2fc
Ranking

Figure 1

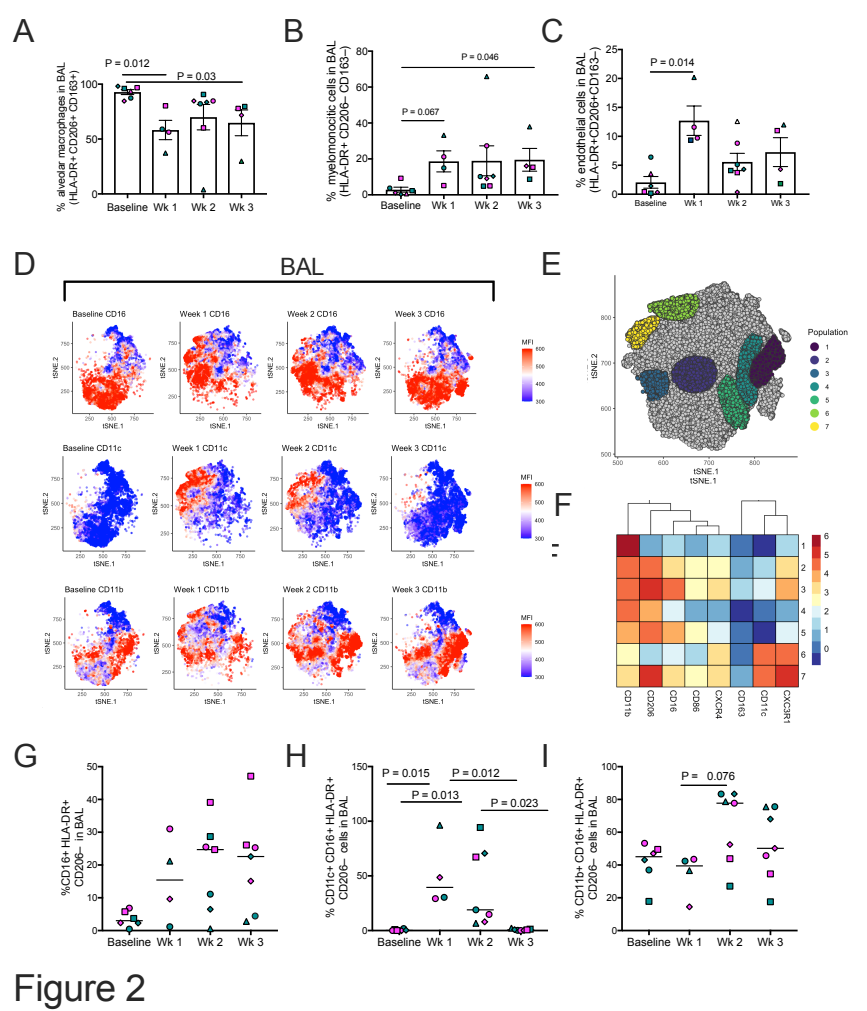
A
P = 0.012
P = 0.03
% alveolar macrophages in BAL (HLA-DR+ CD206+ CD163+)
Baseline
Wk 1
Wk 2
Wk 3
B
P = 0.046
P = 0.067
% myelomonocitic cells in BAL (HLA-DR+ CD206– CD163–)
C
P = 0.014
% endothelial cells in BAL (HLA-DR+CD206+CD163–)
D
BAL
Baseline CD16
Week 1 CD16
Week 2 CD16
Week 3 CD16
Baseline CD11c
Week 1 CD11c
Week 2 CD11c
Week 3 CD11c
Baseline CD11b
Week 1 CD11b
Week 2 CD11b
Week 3 CD11b
tSNE.1
tSNE.2
MFI
E
Population
F
CD11b
CD206
CD16
CD86
CXCR4
CD163
CD11c
CXC3R1
G
%CD16+ HLA-DR+ CD206– in BAL
H
P = 0.015
P = 0.012
P = 0.013
P = 0.023
% CD11c+ CD16+ HLA-DR+ CD206– cells in BAL
I
P = 0.076
% CD11b+ CD16+ HLA-DR+ CD206– cells in BAL

Figure 2

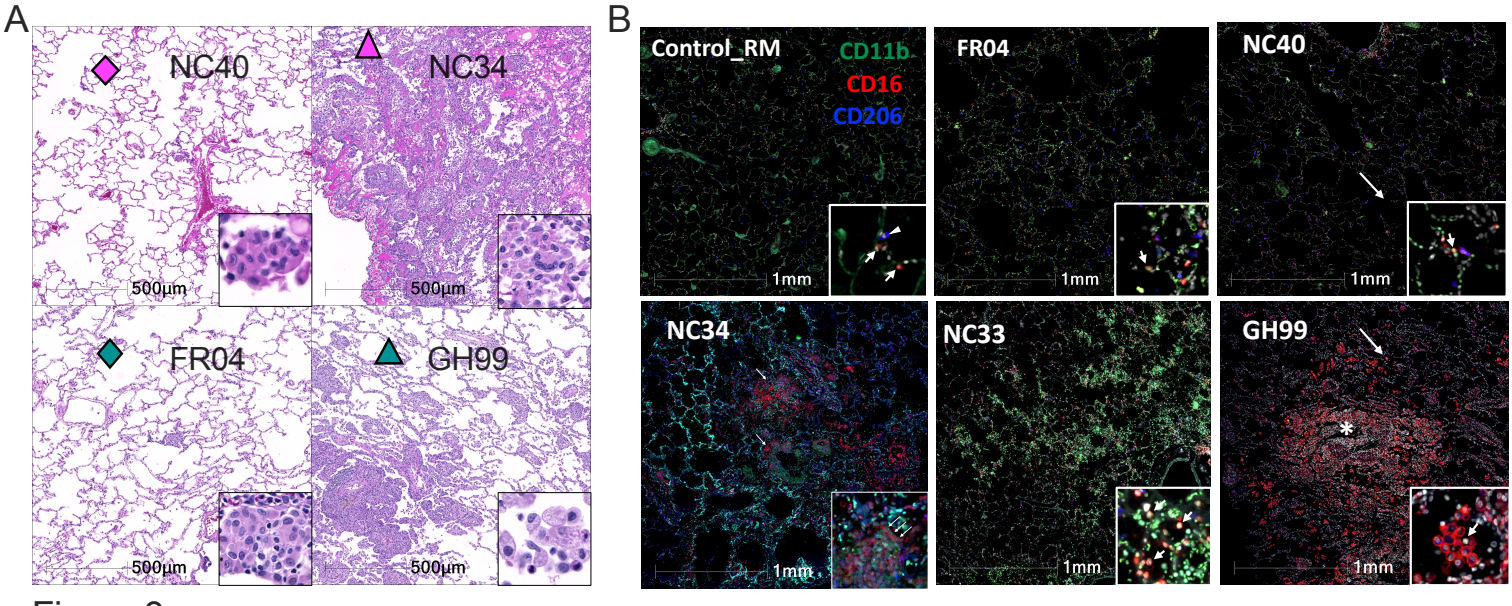
A
NC40
NC34
FR04
GH99
500µm
500µm
500µm
500µm
B
Control_RM
CD11b
CD16
CD206
FR04
NC40
NC34
NC33
GH99
1mm
1mm
1mm
1mm
1mm
1mm

Figure 3

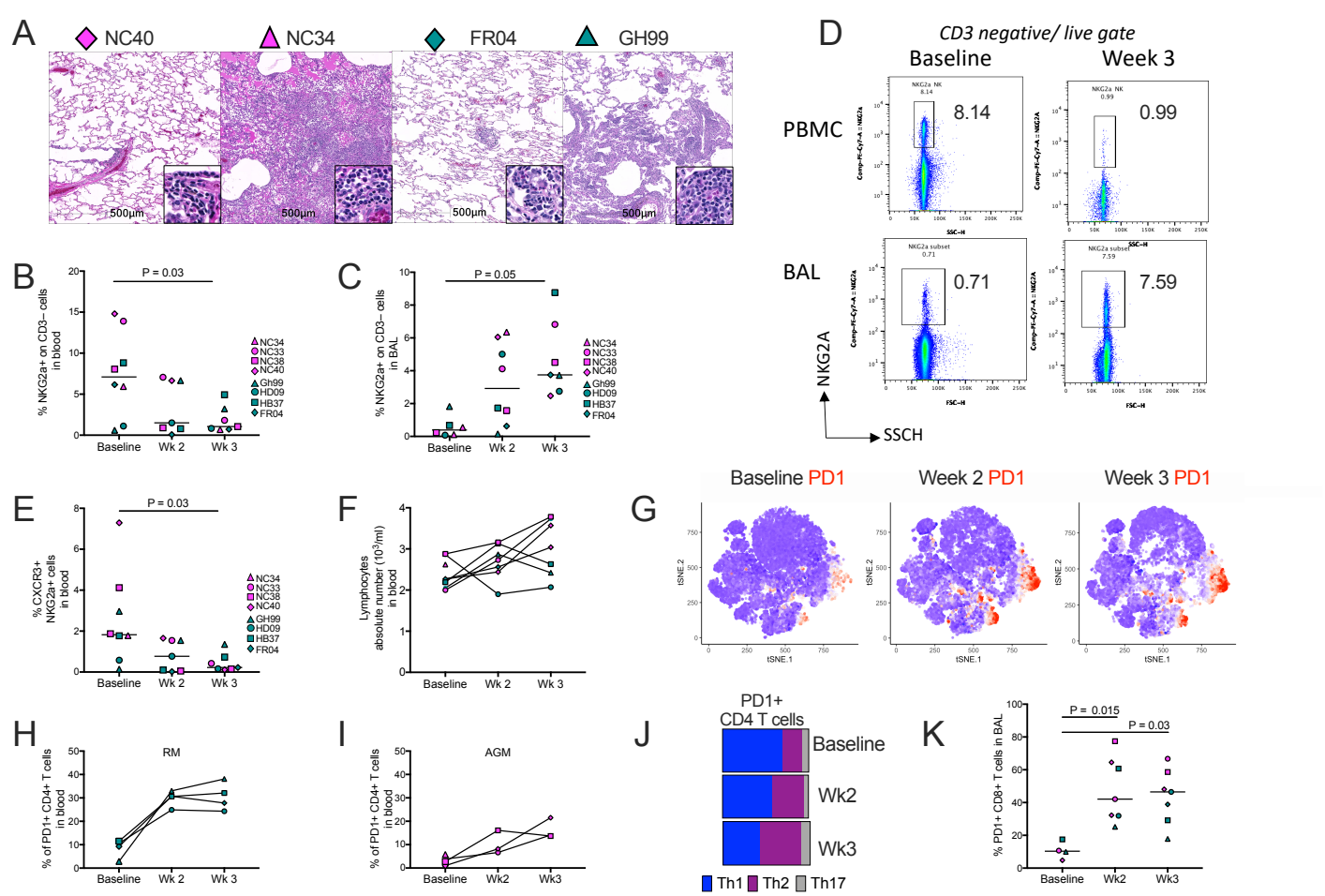
A
NC40
NC34
FR04
GH99
500µm
B
P = 0.03
% NKG2a+ on CD3– cells in blood
Baseline
Wk 2
Wk 3
NC34
NC33
NC38
NC40
Gh99
HD09
HB37
FR04
C
P = 0.05
% NKG2a+ on CD3– cells in BAL
D
CD3 negative/ live gate
Baseline
Week 3
PBMC
BAL
8.14
0.99
0.71
7.59
NKG2A
SSCH
E
P = 0.03
% CXCR3+ NKG2a+ cells in blood
F
Lymphocytes absolute number (10³/ml) in blood
G
Baseline PD1
Week 2 PD1
Week 3 PD1
tSNE.1
tSNE.2
H
RM
% of PD1+ CD4+ T cells in blood
I
AGM
Wk2
Wk3
J
PD1+ CD4 T cells
Baseline
Wk2
Wk3
Th1
Th2
Th17
K
P = 0.015
P = 0.03
% PD1+ CD8+ T cells in BAL

Figure 4

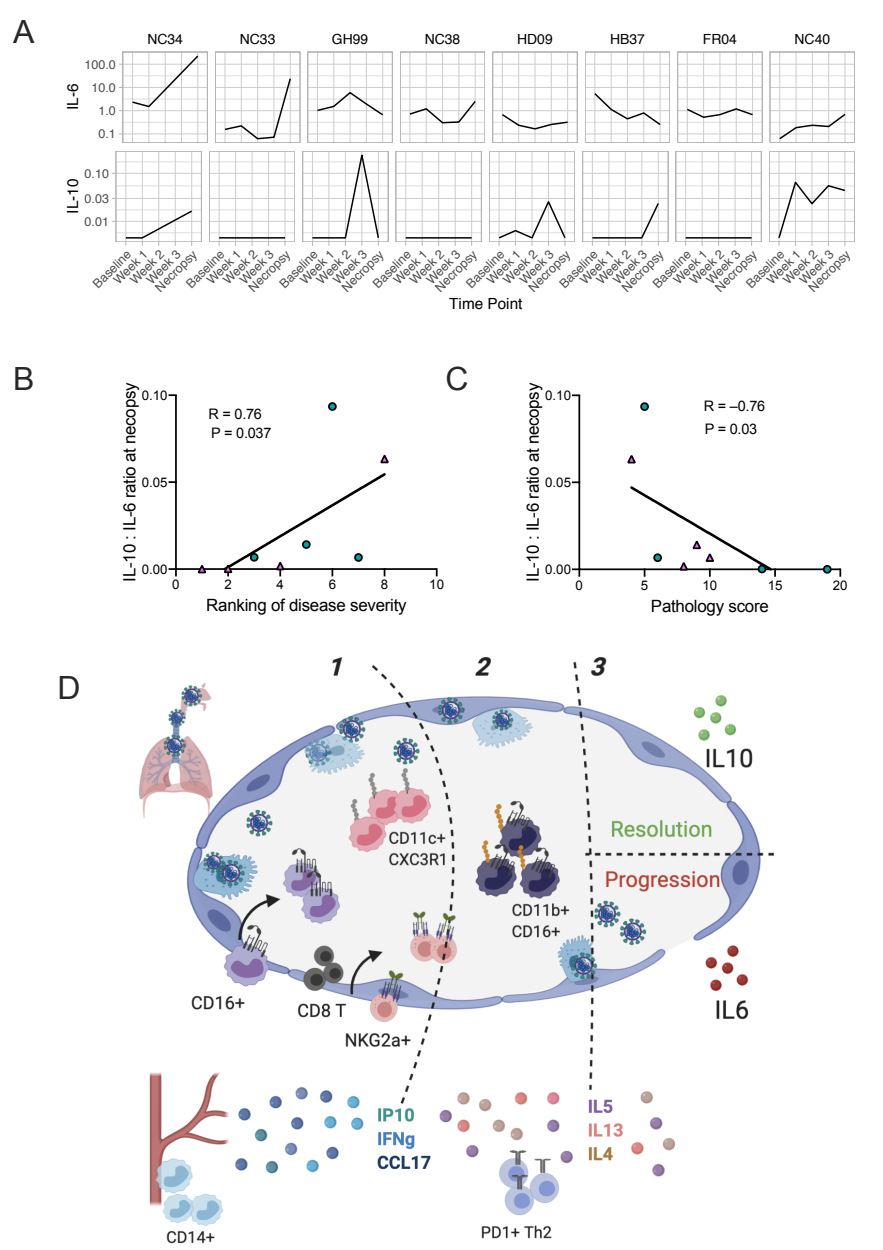
A
NC34
NC33
GH99
NC38
HD09
HB37
FR04
NC40
IL-6
100.0
10.0
1.0
0.1
IL-10
0.10
0.03
0.01
Baseline
Week 1
Week 2
Week 3
Necropsy
Time Point
B
R = 0.76
P = 0.037
IL-10 : IL-6 ratio at necopsy
Ranking of disease severity
C
R = –0.76
P = 0.03
IL-10 : IL-6 ratio at necopsy
Pathology score
D
1
2
3
IL10
Resolution
Progression
CD11c+
CXC3R1
CD11b+
CD16+
CD16+
CD8 T
NKG2a+
IL6
IP10
IFNg
CCL17
IL5
IL13
IL4
CD14+
PD1+ Th2

Figure 5

Supplementary Table 1: Breakdown of routes of exposure and viral inoculation

Animal ID	Exposure (dose)	Age	Sex	Species	Base Weight (kg)
GH99	Cumulative dose of 3.61×10^6 PFU including oral, intratracheal, intranasal, and conjunctival (both eyes)	13.9	Male	*Macaca mulatta*, Indian ancestry	15.5
HD09		12.87	Female	*Macaca mulatta*, Indian ancestry	7.7
NC40		16 (est)	Male	*Chlorocebus aethiops*	7.0
NC33		16 (est)	Female	*Chlorocebus aethiops*	3.7
HB37	Aerosol (approx. 2.0×10^3 $TCID_{50}$)	12.96	Male	*Macaca mulatta*, Indian ancestry	11.9
FR04		14.93	Male	*Macaca mulatta*, Indian ancestry	12.3
NC34		16 (est)	Female	*Chlorocebus aethiops*	4.3
NC38		16 (est)	Male	*Chlorocebus aethiops*	7.4

Ages of monkeys NC40, NC33, NC34, and NC38 are approximate.

Supplementary Table 2: Virus loads in clinical specimens

Week 1

Specimen	HB37	FR04	NC38	NC34	NC33	NC40	GH99	HD09
Bronchial Brush	4.99E+05	1.64E+04	5.81E+06	3.22E+07	4.65E+06	1.42E+06	1.26E+07	1.23E+04
Buccal Swab	3.67E+03	4.74E+04	Not Detected	1.66E+06	Not Detected	1.07E+04	Inconclusive	2.55E+03
Nasal Swab	1.41E+06	1.52E+08	1.94E+04	6.45E+07	1.29E+05	1.05E+07	4.42E+04	1.42E+09
Pharyngeal Swab	5.03E+04	2.12E+06	2.47E+11	2.36E+09	7.00E+06	1.15E+08	Inconclusive	6.54E+06
Rectal Swab	3.81E+03	9.90E+05	4.95E+03	4.32E+03	1.73E+07	6.22E+08	8.22E+03	Not Detected
Vaginal Swab	Not Tested	Not Tested	Not Tested	3.03E+05	5.16E+04	Not Tested	Not Tested	Not Detected

Week 2

Specimen	HB37	FR04	NC38	NC34	NC33	NC40	GH99	HD09
Bronchial Brush	Inconclusive	2.46E+03	2.16E+04	Not Tested	2.92E+06	6.87E+03	1.95E+03	Inconclusive
Buccal Swab	Not Tested	1.71E+04	Inconclusive	Not Tested	6.40E+03	6.95E+03	3.78E+04	Not Detected
Nasal Swab	Not Tested	5.78E+06	2.07E+04	Not Tested	3.27E+06	9.54E+04	1.03E+05	2.89E+03
Pharyngeal Swab	3.77E+04	3.11E+03	5.61E+04	Not Tested	1.45E+03	9.21E+04	4.65E+03	Inconclusive
Rectal Swab	2.63E+04	1.55E+08	4.69E+05	Not Tested	3.93E+09	1.11E+05	2.71E+04	Not Detected
Vaginal Swab	Not Tested	Not Tested	Not Tested	Not Tested	8.92E+04	Not Tested	Not Tested	Not Detected

Week 3

Specimen	HB37	FR04	NC38	NC34	NC33	NC40	GH99	HD09
Bronchial Brush	Not Detected	Inconclusive	1.12E+05	Not Tested	3.04E+07	1.41E+06	Not Detected	Not Detected
Buccal Swab	Not Detected	Inconclusive	Inconclusive	Not Tested	Not Detected	Not Detected	Not Detected	Not Detected
Nasal Swab	Not Detected	7.53E+04	2.67E+04	Not Tested	2.77E+05	1.42E+07	2.03E+04	4.13E+04
Pharyngeal Swab	Not Tested	Not Detected	Not Detected	Not Tested	1.05E+04	8.95E+04	Inconclusive	4.28E+04
Rectal Swab	Not Detected	1.31E+04	3.78E+06	Not Tested	1.45E+04	3.45E+04	Not Detected	Not Detected
Vaginal Swab	Not Tested	Not Tested	Not Tested	Not Tested	Inconclusive	Not Tested	Not Tested	Not Detected

Samples which were not tested were due to lack of sample availability.

Supplementary Table 3: Rotation table derived from PCA

	PC1	PC2	PC3	PC4	PC5	PC6	PC7	PC8
Eotaxin	0.51349854	0.144318924	0.04547296	0.10908504	-0.2471479	0.22538446	-0.68436694	-0.3482608
IP-10	-0.25227747	0.559991260	-0.07652314	0.02243312	0.4106839	-0.16189141	0.05487606	-0.6469353
MCP-1	0.11727127	0.519454673	0.49526810	0.25731776	0.2000296	0.44221279	0.14981145	0.3832805
MCP-4	0.51986265	-0.002353372	0.07196805	-0.22069430	-0.2665758	0.11724746	0.67825244	-0.3619612
MDC	0.45844363	-0.050897556	0.21350047	0.37354660	0.2448526	-0.72839142	0.02537330	0.1047317
MIP-1a	0.15406887	0.251746497	-0.77979454	0.47174206	-0.1062296	0.09007799	0.16325863	0.1903004
MIP-1b	0.39295357	-0.047373837	-0.29263668	-0.51006598	0.6544815	0.14743768	-0.10172114	0.1926359
TARC	0.01858282	0.572304116	-0.04804510	-0.50043369	-0.3994979	-0.39152001	-0.09228374	0.3130139

All elements used for PCA shown.
PC = Principal Component

Supplementary Table 4: Antibodies used in flow cytometry and immunofluorescent microscopy panels

Antibodies used for flow cytometry

Marker	Fluorochrome	Clone	Ref.	Company	Known Reactivity
PD-1	APC	EH12.2H7	329908	Biolegend	RM & AGM
CD56	Alexa 700	B159	557919	BD	RM _ AGM not reported
CD183 (CXCR3)	APC/Cyanine7	G025H7	353722	Biolegend	RM & AGM
CD196 (CCR6)	BV605	G034E3	353420	Biolegend	RM & AGM
CD4	BV797	L200	563914	BD	RM & AGM
CD3	PE	SP34-2	552127	BD	RM & AGM
CD3	BV650	SP34-2	563918	BD	RM & AGM
CD20	BV650	2H7	563780	BD	RM & AGM
CD95	PE/Cyanine5	DX2	559773	BD	RM & AGM
CD8a	Texas Red	RPA-T8	MHCD0817	Life technology	RM & AGM
CD159a (NKG2a)	PE/Cyanine7	Z199	B10246	Beck Coulter	RM & AGM
CD16	BV711	3G8	563127	BD	RM & AGM
CD16	BUV496	3G8	564653	BD	RM & AGM
CD86	FITC	FUN-1	557343	BD	RM _ AGM not reported
CD11c	APC	3.9	17-0116-42	eBioscence	RM & AGM
HLA-DR	APC/Cyanine7	L243	307618	Biolegend	RM & AGM
CD14	V450	M5E2	561390	BD	RM & AGM
CD163	BV711	GHI/61	563889	BD	RM _ AGM not reported
CD184 (CXCR4)	PECF594	12G5	562389	BD	RM & AGM
CD45	BV786	D058-1283	563861	BD	RM & AGM
CX3CR1	PE	K0124E1	355704	Biolegend	RM _ AGM not reported
CD11b	PE/Cyanine5	ICRF44	301308	Biolegend	RM & AGM
CD206	PE/Cyanine7	19.2	25-2069-42	BD	RM & AGM

Antibodies used for immunofluorescent microscopy

Primary Antibody	Species	Company	Ref.	Dilution	Secondary Antibody
CD206	Goat	R&D	AF2535	1:50	Donkey anti-goat 647 (far red)
CD11b	Rabbit	Abcam	Ab133357	1:20	Donkey anti-rabbit 488 (green)
CD16	Mouse IgG2a	Novocastra	NCL-CD16	1:40	Permanent Red
DAPI	Dye - N/A	Invitrogen	D1306	1:20,000	N/A

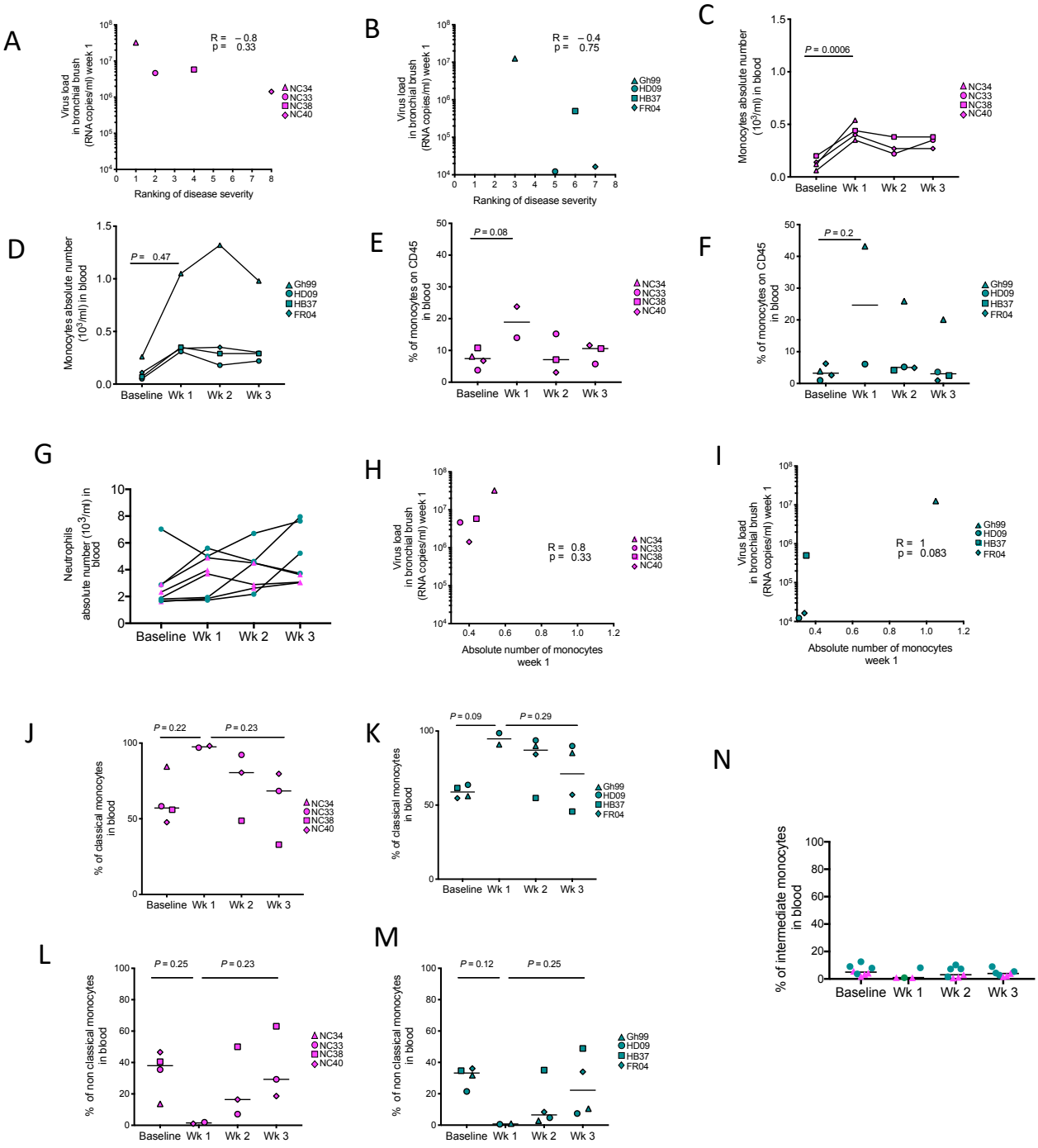

Supplementary Figure 1. Kinetics of monocytes in Rhesus Macaques and African Green Monkeys. Association between SARS-CoV-2 load in bronchial brushes and ranking of disease severity in AGM (**A**) and RM (**B**) (most severe case = 1; mildest case = 8). Changes in monocyte count in blood before and after infection in AGM (**C**) and RM (**D**). Proportion of total monocytes (HLA-DR+ CD16+ and/or CD14+ out of CD45+ leukocytes) in PBMCs from AGM (**E**) and RM (**F**) over time. (**G**) Changes in the absolute number of neutrophils in blood over time in all eight animals. Correlation between SARS-CoV-2 viral load in bronchial brushes and absolute count of monocytes in blood at one-week post-infection (1wk pi) in AGM (**H**) and RM (**I**). Percent of classical (CD14+ CD16–) monocytes (CD14– CD16+) out of total monocytes in PBMCs from AGM (**J**) or RM (**K**). Percent of non classical monocytes (CD14– CD16+) out of total monocytes in PBMCs in AGM (**L**) or RM (**M**). (**N**) Percent of intermediate monocytes (CD14+ CD16+) out of total monocytes in PBMCs from all eight animals over time.

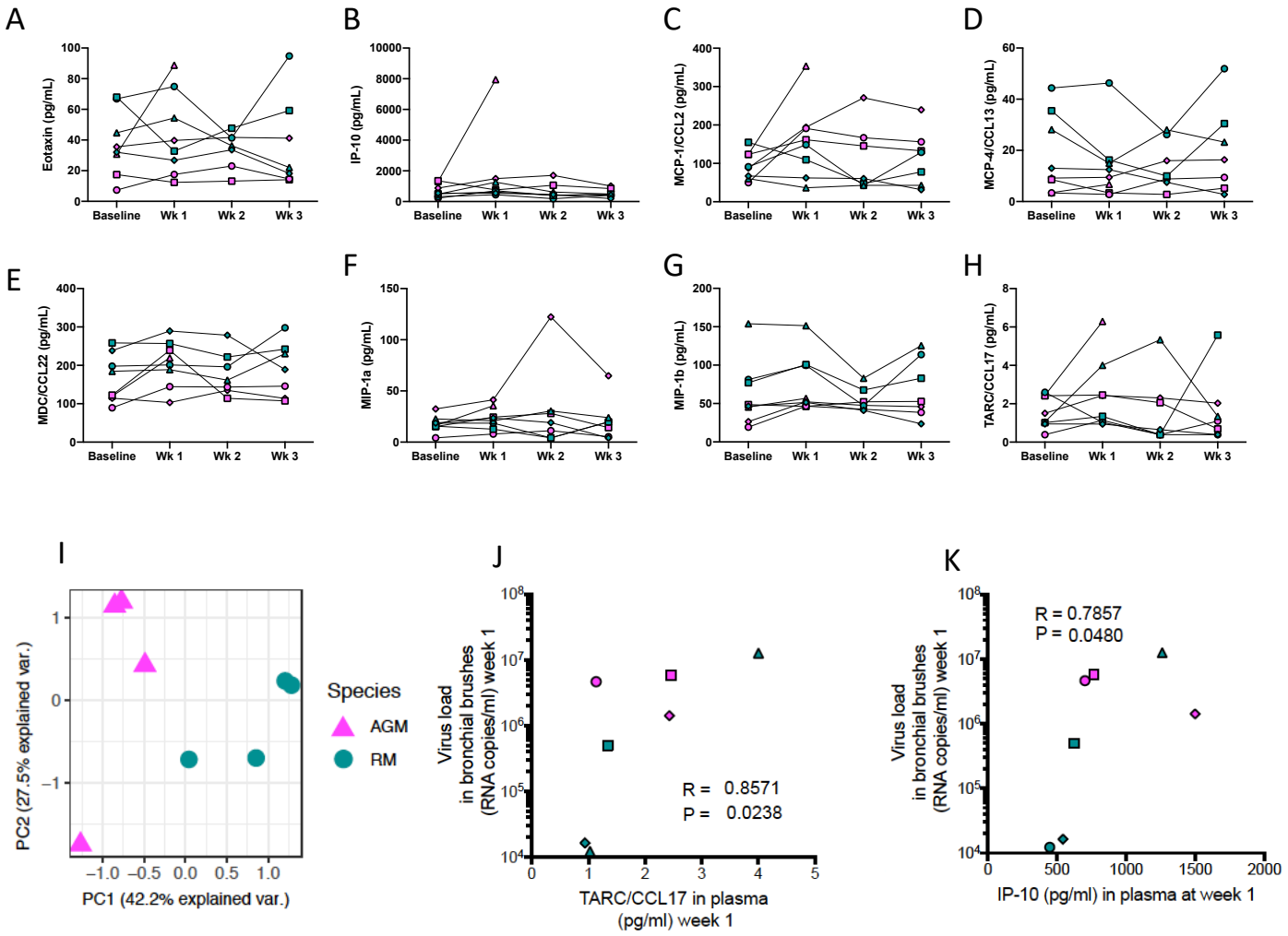

Supplementary Figure 2. Chemokines promote cell migration of monocytes from the blood to the lung following infection. Levels of chemokines in the peripheral blood over time, including (**A**) Eotaxin, (**B**) IP-10, (**C**) MCP-1 (CCL2), (**D**) MCP-4 (CCL13), (**E**) MDC (CCL22), (**F**) MIP-1a, (**G**), MIP-1b, and (**H**) TARC (CCL17). (**I**) PCA plot comparing baseline levels of chemokines between rhesus macaques and African Green monkeys. (**J**) TARC (CCL17) levels and **(K)** IP-10 levels in blood and SARS-CoV-2 viral load in bronchial brushes one week post-infection.

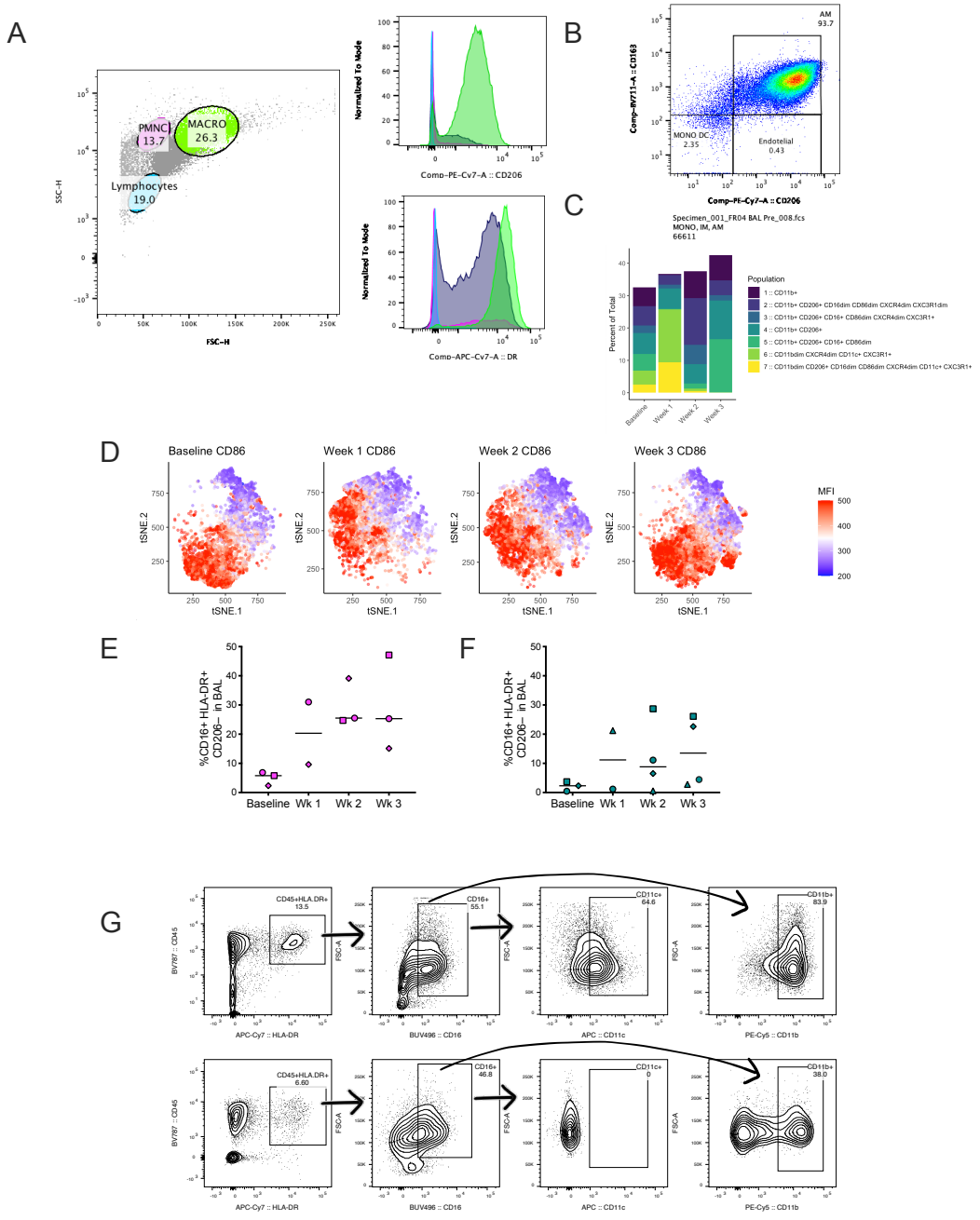

Supplementary Figure 3. Changes in the frequency of alveolar macrophages and infiltrates in BAL during infection by flow cytometric analysis. (**A**) **Left panel.** Representative light scatter (forward scatter and side scatter) analysis of lymphocytes, macrophages, and polymorphonuclear cells (PMNC) in BAL. Cell populations are located according to their relative size (forward scatter) and granularity (side scatter). **Right panels.** Overlaid histograms showing fluorescent intensities of CD206 and HLA-DR of lymphocytes, macrophages, and PMNC as shown on the left panels. (**B**) Representative pseudocolor dot plot displaying alveolar macrophages, endothelial cells, monocytes, and/or dendritic cells distinguished by differential expression of CD163 and CD206. (**C**) Range of phenotypes of CD11b+ and CD11c+ myeloid cells in BAL and their change in proportion out of total HLA-DR+ cells over time. (**D**) tSNE plot displaying kinetics of CD86 expression on total HLA-DR+ cells after infection. Percent of CD16+ HLA-DR+ CD206- cells in BAL over time in AGM (**E**) and RM (**F**). (**G**) Representative gating strategy showing classification of CD45+HLA-DR+CD16+ myeloid cells which express either CD11c or CD11b. Top panel showing a sample with CD11c+ cells, and bottom panel showing a sample without CD11c+ cells used to help determine optimal gate position.

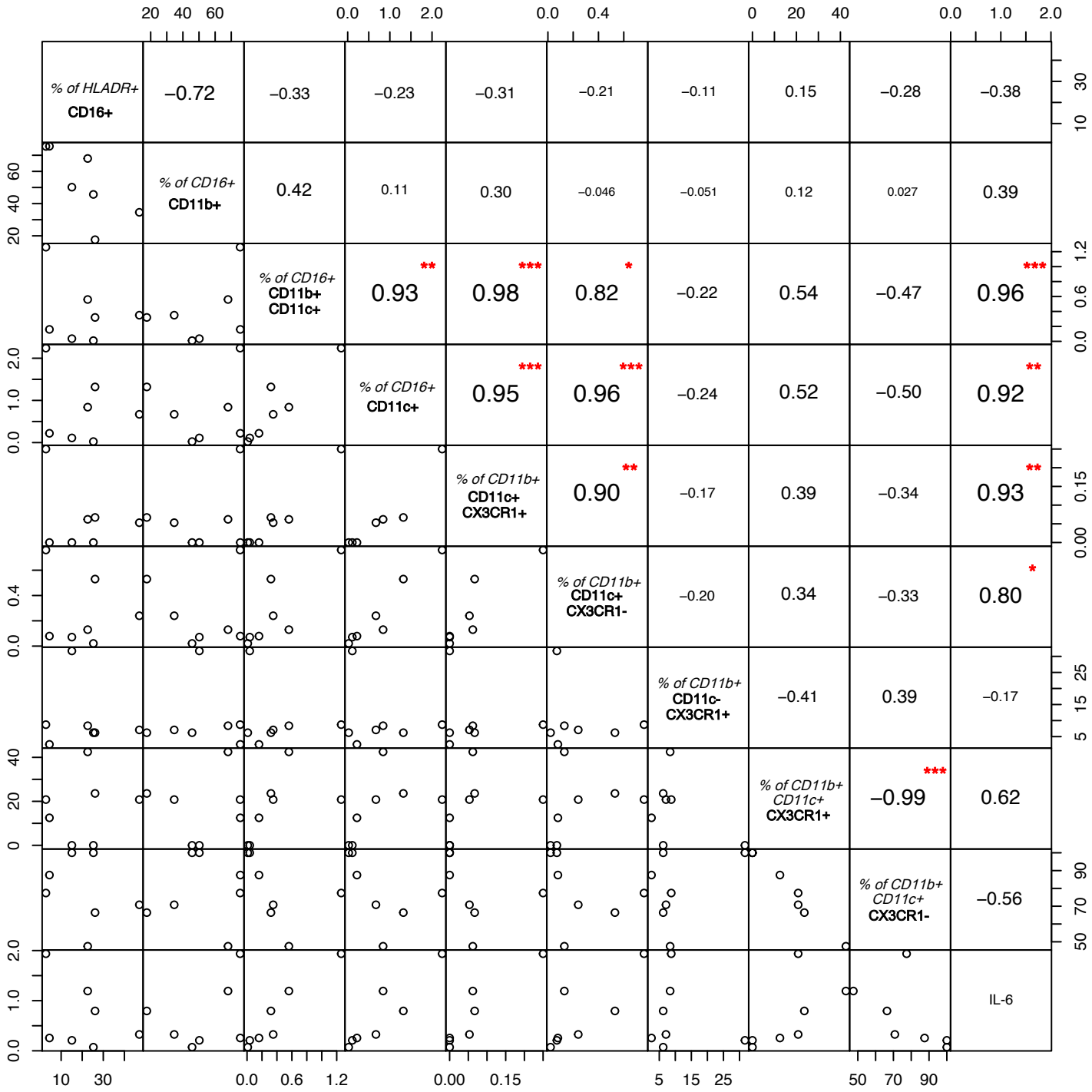

Supplementary Figure 4. Association of myeloid subsets in the BAL with IL-6 plasma levels. Correlation plot between myeloid subsets in BAL and levels of IL-6 (pg/mL) in the blood 3 weeks post infection using Pearson's method. Numbers inside boxes on the diagonal right half of the correlation plot represent the coefficient of correlation (*r*) and asterisks denote significance. One red asterisk corresponds with p <. 05, two red asterisks correspond with p < .01, and three red asterisks correspond with p < .001. Correlation plots in the bottom left display the actual data points.

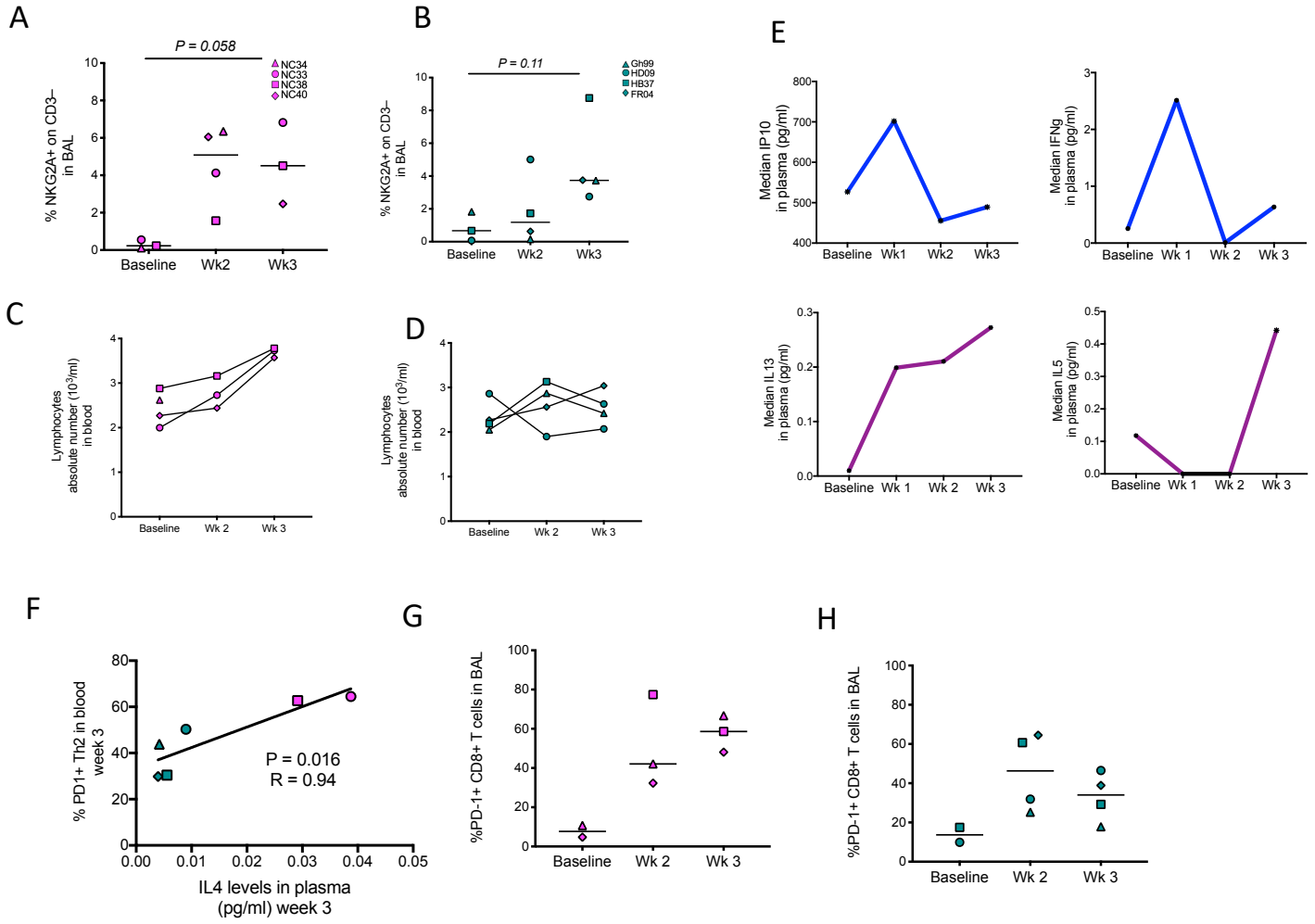

Supplementary Figure 5. Lymphocyte response to SARS-CoV-2 in Rhesus Macaques and African Green Monkeys. Percent of NKG2a+ on CD3- cells in BAL in AGM (**A**) and RM (**B**). Changes in lymphocyte count in blood before and after infection in AGM (**C**) and RM (**D**). (**E**) Median levels of IP-10, IFN-γ, IL-13, and IL-5 in plasma (pg/mL) from all eight animals over time. (**F**) Correlation between IL-4 levels in the plasma (pg/mL) and percent of PD-1+ Th2 cells in the blood at week 3 post infection. Proportion of PD-1+ CD8+ T cells in BAL from AGM (**G**) and RM (**H**) after infection.